

Multiband (X, C, L) radar amplitude analysis for a mixed sand- and gravel-bed river in the eastern Central Andes

Benjamin Purinton*, Bodo Bookhagen

Institute of Geosciences, University of Potsdam, Karl-Liebknecht-Str. 24-25, Potsdam-Golm 14476, Germany



ARTICLE INFO

Edited by Marie Weiss

Keywords:

SAR amplitude
Radar backscatter
Surface roughness
Fluvial geomorphology
TerraSAR-X/TanDEM-X
Sentinel-1
ALOS-2 PALSAR-2

ABSTRACT

Synthetic Aperture Radar (SAR) amplitude measurements from spaceborne sensors are sensitive to surface roughness conditions near their radar wavelength. These backscatter signals are often exploited to assess the roughness of plowed agricultural fields and water surfaces, and less so to complex, heterogeneous geological surfaces. The bedload of mixed sand- and gravel-bed rivers can be considered a mixture of smooth (compacted sand) and rough (gravel) surfaces. Here, we assess backscatter gradients over a large high-mountain alluvial river in the eastern Central Andes with aerially exposed sand and gravel bedload using X-band TerraSAR-X/TanDEM-X, C-band Sentinel-1, and L-band ALOS-2 PALSAR-2 radar scenes. In a first step, we present theory and hypotheses regarding radar response to an alluvial channel bed. We test our hypotheses by comparing backscatter responses over vegetation-free endmember surfaces from inside and outside of the active channel-bed area. We then develop methods to extract smoothed backscatter gradients downstream along the channel using kernel density estimates. In a final step, the local variability of sand-dominated patches is analyzed using Fourier frequency analysis, by fitting stretched-exponential and power-law regression models to the 2-D power spectrum of backscatter amplitude. We find a large range in backscatter depending on the heterogeneity of contiguous smooth- and rough-patches of bedload material. The SAR amplitude signal responds primarily to the fraction of smooth-sand bedload, but is further modified by gravel elements. The sensitivity to gravel is more apparent in longer wavelength L-band radar, whereas C- and X-band is sensitive only to sand variability. Because the spatial extent of smooth sand patches in our study area is typically < 50 m, only higher resolution sensors (e.g., TerraSAR-X/TanDEM-X) are useful for power spectrum analysis. Our results show the potential for mapping sand-gravel transitions and local geomorphic complexity in alluvial rivers with aerially exposed bedload using SAR amplitude.

1. Introduction

High-mountain rivers act as the drains of orogenic belts by transporting eroded rock material from hillslopes downstream as detritus in mixed sand and gravel bedload. The characteristics of this sediment, and the geological deposits they form, hold keys to deciphering drivers of mountain building and erosion (e.g., Strecker et al., 2007; Attal et al., 2015; Dingle et al., 2017). Variation in bedload quantity and grain-size distributions control channel geometry over decadal to millennial timescales (e.g., Sklar et al., 2006; Pfeiffer et al., 2017). This bedload has implications for ecological management (e.g., Kondolf and Wolman, 1993) and provides essential nutrients for agriculture in floodplains. In turn, the impact of human infrastructure on rivers can lead to significant changes in sediment flux (Syvitski et al., 2005) and bedload characteristics (Grant, 2012), with far-reaching implications

(Walter and Merritts, 2008).

As rivers flow downstream, they pass through tectono-geomorphic zones created by the geological, climate, and vegetation settings along with the drainage network connections (e.g., Rice and Church, 1998; Church, 2002; Attal and Lavé, 2006). These zones cause heterogeneous mixtures of sand and gravel bedload, herein referred to as sand-gravel patchiness, which we define as discrete areas on the order of 1–100 m² with similar bedload characteristics dominated by sand, gravel, or some mixture of the two (e.g., Nelson et al., 2009). Low patchiness refers to more mixing of sand and gravel and high patchiness refers to more discrete sand- or gravel-dominated patches (e.g., sand or gravel bars). The arrangement and size of mixed sand and gravel patches can vary significantly over short distances both along- and across-channel, making sampling characteristic grain sizes difficult via traditional measures (e.g., Wolcott and Church, 1991). Digital grain-sizing

* Corresponding author.

E-mail address: purinton@uni-potsdam.de (B. Purinton).

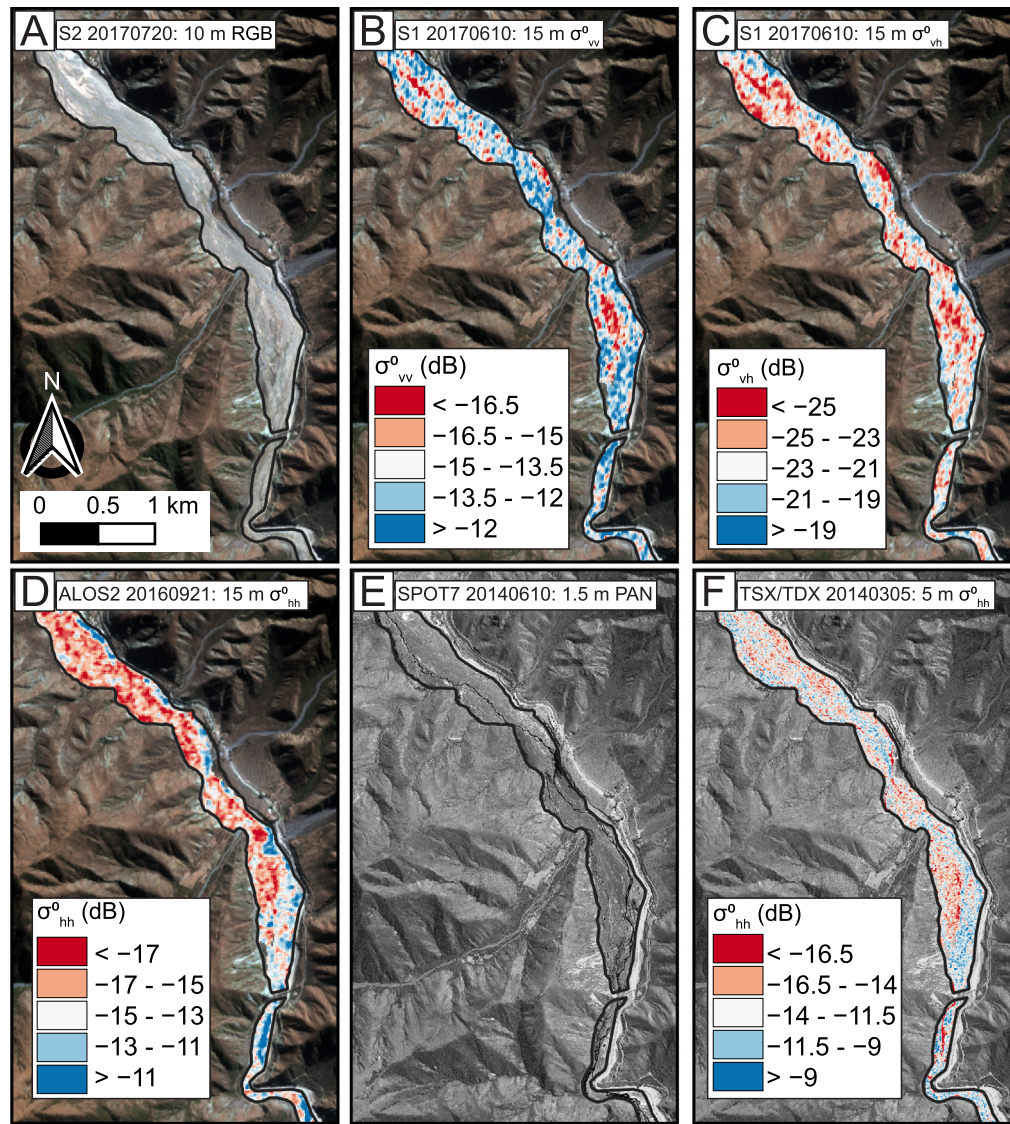


Fig. 1. Comparing optical versus radar data in the study area. The location is indicated in Fig. 2A. (A) shows a Sentinel-2 (S2) RGB composite (bands 2, 3, and 4) with (B), (C), and (D) showing the same 10-m resolution optical scene overlain with 15-m resolution backscatter from S1 σ_{vv}^0 , S1 σ_{vh}^0 , and ALOS2 σ_{hh}^0 , respectively. (E) shows a SPOT7 panchromatic (PAN) gray-scale 1.5-m image for the same area and in (F) the corresponding 5-m TSX/TDX σ_{hh}^0 . All dates are in YYYYMMDD format. The channel (hand-clicked black outline), flows from north to south. Calculation of the backscatter coefficient (σ^0) is described in the Methods and data repository. All color scales are from the 1st-99th percentile of backscatter values in the framed channel area. We note some visible differences in optical reflectance that could be exploited, but point out that the information in the SAR signal is more detailed, with lower (more red) values indicating smoother surfaces and higher (more blue) values indicating rougher surfaces. (For interpretation of the references to color in this figure legend, the reader is referred to the web version of this article.)

techniques for high-mountain rivers are improving (e.g., Purinton and Bookhagen, 2019a, 2019b), but capturing downstream evolution of channel-bedload characteristics (Attal and Lavé, 2006) or gravel-sand transitions (Dingle et al., 2017) at the scale of mountain belts remains challenging.

Herein lies the utility of remote sensing with spaceborne platforms. Specifically, the response of Synthetic Aperture Radar (SAR) backscatter intensity (the amplitude of returned signals) is modulated by a combination of radar-look geometry, surface roughness, and soil-moisture content of the surface (Ulaby et al., 1982; Farr, 1993). Roughness, which dominates returns on unvegetated surfaces (Dierking, 1999), is often defined as either the root mean square of height variations ($Hrms$) and the auto-correlation length (L) within a cell (e.g., Aubert et al., 2011), or, in some cases, as the power spectrum slope and offset from cm-resolution 1-D surface profiles (e.g., Weeks et al., 1996). Although neither method provides perfect characterization of scale-dependent natural roughness (Shepard et al., 2001), empirical and theoretical models between these parameters and SAR backscatter have demonstrated positive relationships (e.g., Dierking, 1999).

Geologic surfaces have been investigated to a limited extent using SAR in dry desert environments by modeling backscatter response to roughness variations on gravelly surfaces (e.g., Evans et al., 1992; Ridley

et al., 1996; Weeks et al., 1996, 1997), comparing backscatter intensity with roughness or grain-size statistics (e.g., Deroïn et al., 1997; Campbell and Shepard, 1996; Campbell, 2001; Williams and Greeley, 2004), and inferring the age of alluvial fan surfaces from backscatter variations (e.g., Farr and Chadwick, 1996; Hetz et al., 2016). However, most recent radar backscatter research has focused on agricultural settings to measure soil roughness and moisture (e.g., Baghdadi et al., 2008, 2018; Rahman et al., 2008; Srivastava et al., 2009; Aubert et al., 2011; Vreugdenhil et al., 2018). Within this, much work has gone into the theoretical and empirical modeling of radar response to rough surfaces in order to retrieve the soil-moisture signals of primary interest to farming (e.g., Baghdadi and Zribi, 2006; Bryant et al., 2007; Verhoest et al., 2008; Gorrab et al., 2015).

Few studies have applied SAR roughness measurements to fluvial environments, and all have been limited to dry desert beds and sparse observations (McCauley et al., 1982; Baade and Schmullius, 2010; Sadeh et al., 2018). In this study, we apply radar backscatter measurements for three radar wavelengths to measure downstream changes in bedload grain size along a 115-km reach stretching from 4.5- to 1-km elevation in the eastern Central Andes. The three sensors used are X-band TerraSAR-X/TanDEM-X (TSX/TDX), C-band Sentinel-1A/B (S1), and L-band ALOS-2 PALSAR-2 (ALOS2), with multilooked ground resolutions of 5, 15, and 15 m, respectively. Our results demonstrate that

different radar wavelengths and spatial resolutions are useful for deciphering sub-pixel roughness and measuring the sand-gravel patchiness of dynamic mountain rivers.

2. Optical versus radar data

Previous research has demonstrated the utility of spaceborne optical data in assessing grain-size information from sub-pixel shadowing (Weeks et al., 1996; Mushkin and Gillespie, 2005, 2006). In this study we focus on radar imagery, because optical techniques are highly dependent on lighting (sun angle) and atmospheric conditions (cloudiness), and require two scenes gathered at the same time from different angles (Mushkin and Gillespie, 2005, 2006). On the other hand, radar data are capable of penetrating cloud cover and can retrieve backscatter information at any time of day and using only one scene. Furthermore, where shadowing is a correlative measure of surface roughness, radar more directly measures the relative height of the surface from reflected amplitude signals. However, radar backscatter data are influenced by several parameters, including vegetation and soil moisture (e.g., Verhoest et al., 2008; Vreugdenhil et al., 2018), thus requiring caution in analysis. The difference between optical and radar data in terms of response contrast over an alluvial channel bed is demonstrated in Fig. 1. Theory behind the observed SAR amplitude response is provided in the next section.

3. Expected SAR amplitude response to channel bed

We consider the mixture of sand and gravel in a dry riverbed as a mix of two endmembers: smooth (sandy) and rough (gravely) surface. The Rayleigh criterion of electromagnetic interaction with surfaces places the smooth-rough transition at approximately $\lambda/(8 * \cos(\theta_i))$, where λ is the radar wavelength and θ_i is the local incidence angle of the wave (Farr, 1993). Where surface roughness is significantly below the radar wavelength, the radar signal reflects off the surface away from the sensor (specular reflection) leading to low backscatter intensity measured (e.g., on compacted sand or calm water bodies). As roughness increases to the scale of the wavelength (e.g., contiguous gravel patches), increasing radiation is scattered back towards the sensor (diffuse reflection) with a nonlinear relationship up to a grain-size plateau beyond which increasing roughness leads to little change in backscattering (i.e., the surface is "saturated"; Campbell and Shepard, 1996). Peake and Oliver (1971) defined two cutoffs for radar-smooth and radar-rough geologic surfaces as $\lambda/(25 * \cos(\theta_i))$ and $\lambda/(4.4 * \cos(\theta_i))$, respectively. These criteria are useful references for expected transitional behavior of the SAR amplitude signal on gravely surfaces (McCauley et al., 1982).

From such considerations we can form hypotheses of SAR response to a patchy sand-gravel riverbed surface at various wavelengths. Since a single spaceborne SAR measurement (e.g., $\sim 5 \times 20$ m in range \times azimuth for S1) may contain a variety of smooth and rough surfaces, we can assume that the backscatter will represent a mixture of specular and diffuse reflections. More sand leads to a more specular, lower intensity reflection and increasing gravel (and arrangement of those gravels in contiguous patches) tends towards a more diffuse, higher intensity reflection. For higher ground resolutions (e.g., $\sim 2 \times 2$ m in range \times azimuth for TSX/TDX) there may be less mixing of sand and gravel in the smaller area allowing for a greater range in amplitude as opposed to more mixed signals from coarser pixels, but this depends on the radar wavelength and the patchiness scale (i.e., the size of contiguous sand- or gravel-dominated bars). In some cases, a single strong scatterer (i.e., a large boulder) in the measurement can cause a strong double-bounce effect from reflection off smoother surfaces amplified strongly by large objects (e.g., Evans et al., 1986; Campbell, 2001), which can dominate the backscatter signal.

Assuming an $\sim 30^\circ$ incidence angle for SAR imagery in X-band ($\lambda = 3.1$ cm), C-band ($\lambda = 5.6$ cm), and L-band ($\lambda = 22.9$ cm), the radar-

smooth and rough thresholds — for X-, C-, and L-band, respectively — are 0.1 and 0.8 cm, 0.3 and 1.5 cm, and 1.1 and 6.0 cm. Aside from fine-gravel or sand-only surfaces, a riverbed tends to have height variations above 1 cm. Therefore, X-band will be sensitive to only changes in relative sand-covered surface area, and the inclusion of gravels in the measured area will lead to rapid signal saturation. On the other hand, C-band may still show some sensitivity to gravel inclusion with a rough-surface threshold of 1.5 cm, although it will primarily respond to the presence or absence of sand-dominated patches. Only the longest wavelength L-band should show sensitivity to a large range in grain sizes < 6 cm, and is therefore most useful for tracking changes in pebble size along a channel.

In a highly active channel bed with little to no vegetation, the only factors influencing backscatter should be roughness and moisture. Soil moisture is known to cause an increase in backscatter intensity (e.g., Verhoest et al., 2008; Gorra et al., 2015; Bousbih et al., 2017) up to very wet conditions ($> 30\%$ moisture), where the relationship has been shown to decrease (Baghdadi et al., 2008). These relationships are from fine-sand and silty soils where water retention is much higher than for granular sand- and gravel-bedded alluvial channels in drier high-mountain environments. Some studies exist on the penetration of radar into loose, dry sand many meters thick on desert dunes (e.g., McCauley et al., 1982; Williams and Greeley, 2004), but we are less concerned with this issue in channel beds where the sand is less dry, compacted to smooth surfaces, and does not reach thickness above ~ 1 m. In a channel bed where the sand is interspersed with frequent pebbles, this penetration will be reduced even more, thus limiting any moisture effects from the deeper water table. These moisture effects may become more important in channel reaches where higher flows are more common and the channel bed is not consistently aerially exposed. The water surface of higher flows may contribute to backscattering in two contrasting ways: (a) a smooth water surface decreases backscatter via specular reflection; and (b) turbid water with high suspended sediment loads and a rough surface increases backscatter via diffuse reflection.

Regarding the effect of SAR polarization, we expect the cross-polarized bands (e.g., vertical-horizontal, or VH, for S1) to exhibit a similar, although lower magnitude, response to gravely and sandy surfaces compared to co-polarized bands (e.g., vertical-vertical, or VV, for S1). It has been previously demonstrated that cross-polarized SAR is most useful for tracking vegetation changes, which cause modulation of the polarization by volume-scattering (e.g., Vreugdenhil et al., 2018). These effects are limited in low-vegetation braided alluvial channels. Given these considerations, we focus our analysis on the co-polarized SAR bands, which should exhibit similar horizontal-horizontal (HH) or VV responses, as the gravel elements cause intensity scattering in both the vertical and horizontal directions.

4. Study area

Previous fieldwork in the Toro Basin of northwest Argentina (Fig. 2) includes: cosmogenic radionuclide measurements of geomorphic rates (Bookhagen and Strecker, 2012; Tofelde et al., 2017), historical record-based estimation of modern hydroclimatic regimes (Castino et al., 2016b), detailed differential GPS surveying (Purinton and Bookhagen, 2017), bedload transport observation and remote sensing measurement (Purinton and Bookhagen, 2018), and channel-bed cross-section photo surveying (Purinton and Bookhagen, 2019a). We have chosen the Río Toro as our study site given the high variability and dynamic nature of the channel demonstrated in these studies. This previous work and field observations over many years provide a detailed framework to assess SAR response to roughness variations in this river. Finally, the data available for X-band (TSX/TDX) and L-band (ALOS2) in the present study were restricted to the Toro Basin (see SAR footprints in Fig. 2A).

The Río Toro flows approximately north to south through a steep environmental, topographic, and rainfall gradient from the upper reaches (~ 3 km elevation) bordering the hyper-arid (rainfall < 0.2 m/

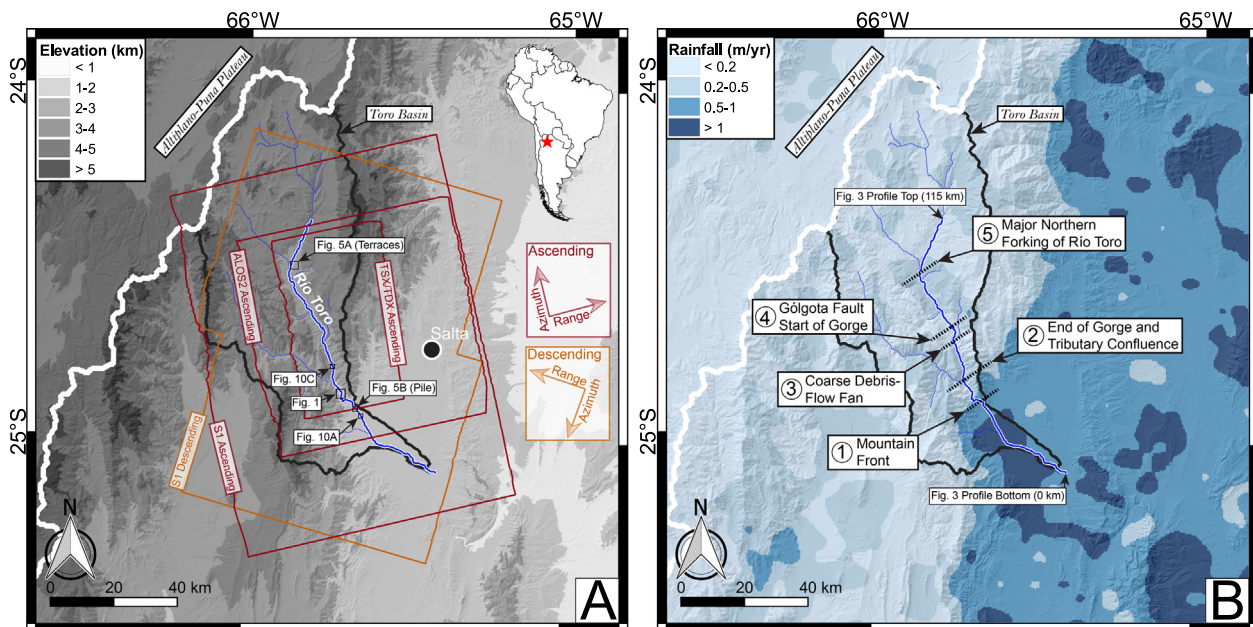


Fig. 2. Overview of the study area. (A) shows the topography of the Toro Basin (thick black outline) in northwest Argentina near Salta, bordering the internally drained Altiplano-Puna Plateau (thick white outline) of the Central Andes. The Río Toro main-stem measurement area (profiled in Fig. 3) is highlighted by the thick blue line, and representative SAR footprints used in this study are shown with orange (descending) and red (ascending) polygons, with the scene azimuth (satellite travel direction) and range (satellite look direction) arrows indicated. The elevation, hillshade, and drainage network is derived from SRTM data (Jarvis et al., 2008). (B) shows the mean annual rainfall over 12 years from the Tropical Rainfall Measurement Mission (TRMM2B31; Bookhagen and Strecker, 2008) to highlight the steep environmental gradient from the arid, sparsely vegetated upper Toro to the humid, vegetated foreland, with orographic moisture blocking indicated by the light (west) versus dark (east) color difference at the mountain front running from south to north. The locations of tectono-geomorphic transitions along the channel are indicated by dashed black lines with the numbers (1–5) used in subsequent plots. (For interpretation of the references to color in this figure legend, the reader is referred to the web version of this article.)

yr), internally drained Altiplano-Puna Plateau (Allmendinger et al., 1997; Bookhagen and Strecker, 2008), down through a zone of large Quaternary fill-terraces (Tofelde et al., 2017), then a narrow bedrock gorge (Hilley and Strecker, 2005), and out through the orographic barrier at the mountain front (rainfall > 1 m/yr), before passing through the Lerma Valley (~1 km elevation). The topographic, climatic, and environmental zones are captured in profile-view along the channel in Fig. 3, showing: rainfall; hillslope and active channel Normalized Difference Vegetation Index (NDVI); and channel-bed slope and width. The active channel is defined by a hand-clicked outline on high-spatial resolution imagery of the low- to non-vegetated channel bed, often constrained by steep valley walls, where bankfull or lower discharge events continuously rearrange bedload. The hillslope area is a buffered region bracketing the active channel 100 m from both banks and 100-m wide on either side of the channel where vegetation is present, water level rarely reaches, and hillslope transport processes dominate.

Within the braided gravel-bedded active channel, high-intensity rainfall events, particularly during the summer monsoon season (Castino et al., 2016a, 2016b, 2017), lead to flooding and bedload transport between longer periods of low-flow and bedload aerial exposure. Vegetation in the active channel is limited because of the high bedload transport (Purinton and Bookhagen, 2018), although in the more arid, but low-slope, upstream reaches there are some scattered (~2–10 m separated), low (~0.5–1.5 m tall) bushes in the channel, which cause local increases in NDVI (Fig. 3B).

The characteristics of the Río Toro are shown with the inset field photos P1–8 in Fig. 3A. The upstream reach contains many smooth sandy surfaces (P8) transitioning to highly mixed sand and gravel surfaces over the majority of the studied reach (P3–7). Over most of the channel, there are few large (> 1 m) boulders, and a typically uniform distribution of < 50-cm clasts mixed with sandy patches dominates. Downstream of the mountain front the water surface may locally cover

a large proportion of the channel bed (P2) with an armored surface, possibly related to anthropogenic gravel mining (Purinton and Bookhagen, 2018), occurring in some locations as sand is more easily transported during the higher flow periods. These intermittent higher flows are caused by orographic rainfall (Bookhagen and Strecker, 2008) and, to a lesser extent, diurnal variation in groundwater levels.

The aerial photos in Fig. 4 show a typical channel reach upstream of the mountain front, making a few things about the setting apparent. Firstly, the water surface typically accounts for < 5–10% of the channel-bed width. The remaining aerially exposed bed quickly dries during sunshine hours in the high-elevation subtropical catchment after infrequent storms clear the mountain-front barrier (i.e., the gravel surfaces are dry to the touch shortly after rainfall, and thus moisture content is expected to have low impact on SAR backscatter). These photos also show that gravel and sand patches in the active channel generally have low anisotropy (i.e., there are few elongated pure sand- or gravel-dominated bars), with the channel-bed instead showing highly mixed sand and gravel patches with frequent changes in the grain-size distribution over < ~10-m distances. High anisotropy of sand and gravel arrangements would exist where along-channel elongated bars of either all gravel or all sand were present, but this is less common in the Río Toro, likely because the steep setting and high delivery of tributary and hillslope (e.g., landslide) material leads to high across-stream sediment transport rates and a more chaotic arrangement.

5. Methods

We processed the SAR images to reduce sensor noise, correct for terrain distortion, and provide logarithmic amplitude measurements in units of dB on coincident rasters with the final spatial resolution determined by the raw sensor resolution. We are interested in exploiting differences in backscatter amplitude along the channel to measure

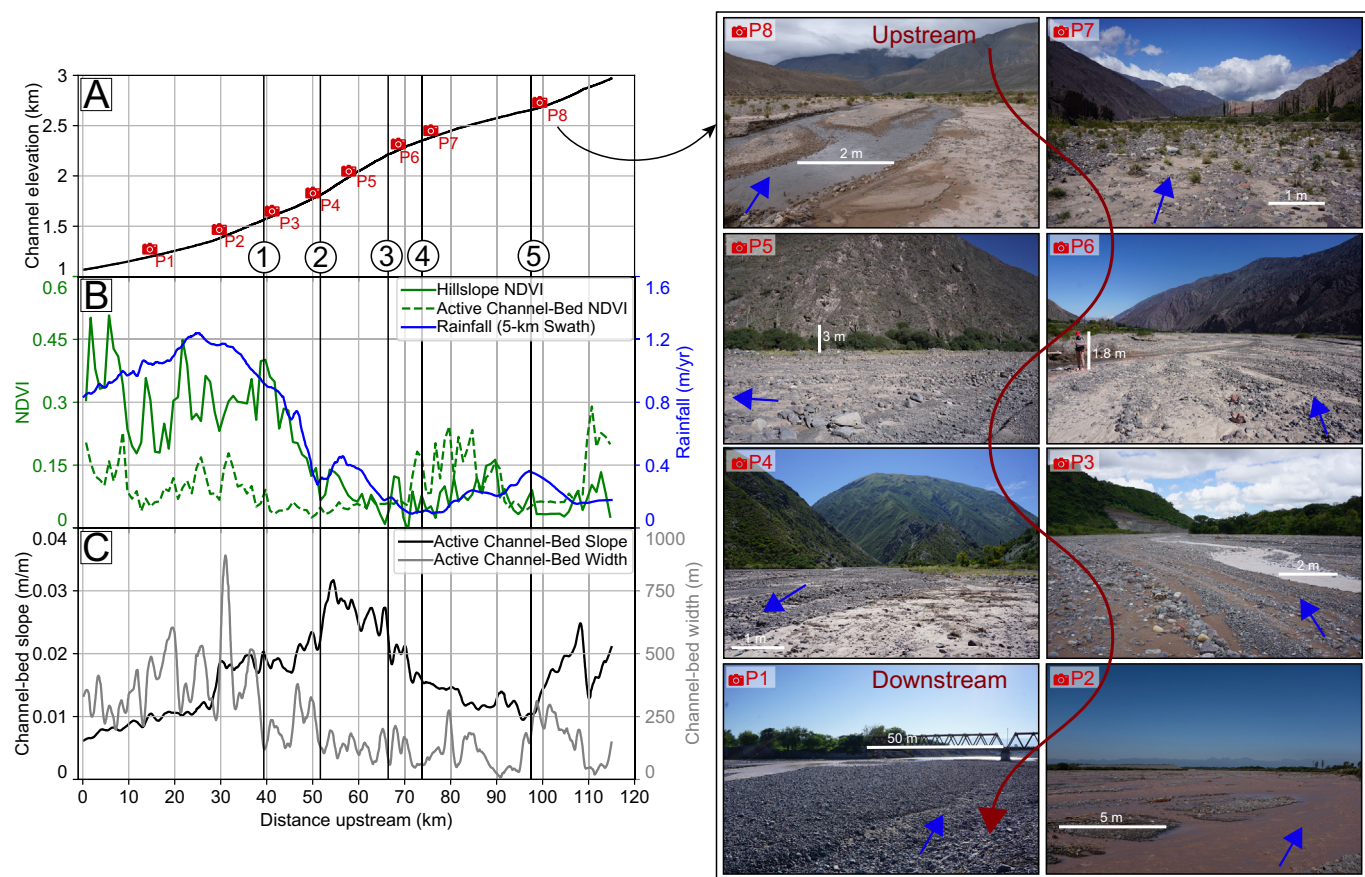


Fig. 3. Topographic, climatic, and environmental characteristics of the Río Toro in profile. (A) shows the elevation profile. (B) shows mean TRMM2B31-derived rainfall in a 5-km-wide swath along profile, and the mean active channel and hillslope Normalized Difference Vegetation Index (NDVI) in 1-km bins along the channel. (C) shows the channel-bed slope and width, both smoothed using a Savitzky-Golay filter with a second-order polynomial and a window length of 3 km. The tectono-geomorphic transitions (1–5) correspond to Fig. 2B. Inset field photos P1–8 in (A) show the nature of the sand and gravel arrangement in the active channel (flow direction given by blue arrow). Note the steepening of the channel downstream of (4) where the Gólgota fault (Marrett et al., 1994) crosses the channel and creates a broad knickzone leading into a high-relief bedrock gorge, where many small tributaries and steep hillslopes deliver material with a large range in grain size to the channel bed, such as the debris-flow fan at (3). Following the confluence of the large tributary at (2), where the gorge ends, the channel shallows and widens. Shallowing and widening increase downstream of the mountain front at (1) and out into the foreland, with corresponding increases in rainfall and vegetation (mostly farmland, with intermittent dense tree stands) outside of the channel bed. (For interpretation of the references to color in this figure legend, the reader is referred to the web version of this article.)

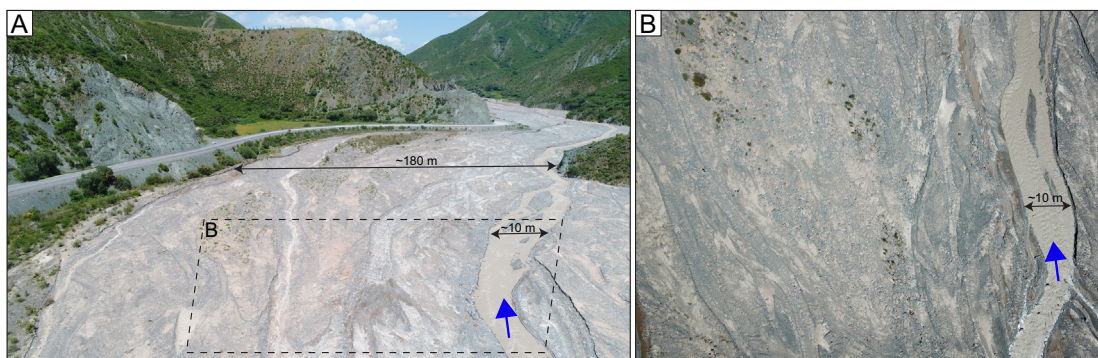


Fig. 4. Pictures of the Río Toro (flow direction given by blue arrow) upstream of the mountain front captured with an unmanned aerial vehicle (UAV) at the same location as P4 in Fig. 3. (A) shows an oblique view and (B) shows a top-down view with the location indicated in (A). The pictures were captured with one-year separation, leading to some differences in the channel bed, but the main flow path (river-water surface) remained stable in this period. Some cloud buildup can be seen in the distance in (A) at the mountain front, but note the clear skies upstream, where the intense sunshine dries previously wetted channel bed and causes low moisture away from flowing water. The water surface is narrow with respect to the wide, dry active channel bed. Elongated sand- or gravel-dominated bars are sometimes present, but there are frequent changes in the grain-size distribution over short distances and generally well-mixed gravel and sand arrangements at scales > 10 m. (For interpretation of the references to color in this figure legend, the reader is referred to the web version of this article.)

changes in surface roughness related to sub-pixel sand and gravel arrangements affecting specular to diffuse radar reflection. The channel bed contains only sparse large boulders (> 1 m) that would cause a strong double-bounce effect. Therefore, we expect limited influence of single strong scatterers dominating the signal at any given pixel, and differences in backscatter amplitude instead represent the mixture of smoother (sand) and rougher (gravel) patches. In the following, we outline the processing of each step in the analysis, with some additional details contained in the data repository.

5.1. Data processing

In the X-band, we used 12 TSX/TDX HH polarized stripmap scenes (Krieger et al., 2007), with eight from descending passes and four from ascending, all processed to 5-m ground resolution with 2×2 (range \times azimuth) multilooking. The C-band data are from S1 VV and VH polarized sensors in stripmap mode (Torres et al., 2012), with 15 scenes separated into five descending and 10 ascending, processed to 15-m ground resolution using 4×1 multilooking. Finally, we have three L-band scenes from the ALOS2 HH and HV polarized sensor (Kankaku et al., 2013), all from ascending passes, also processed to 15-m ground resolution using 5×2 multilooking. A table with scene dates can be found in the data repository (Table DR1).

All SAR data were received in L1 Single Look Complex (SLC) format and processed to square gridded pixels using the Sentinel Application Platform (SNAP) (SNAP, 2019). This included radiometric calibration, speckle smoothing, multilooking, and terrain correction to output backscatter rasters in σ^0 format. We converted γ^0 to the local incidence angle corrected σ^0 value, where $\sigma^0 = \gamma^0 * \cos(\theta_i)$ (Small, 2011), expressed in dB format, where $dB = 10 * \log_{10}(\sigma^0)$. The full processing steps are listed in the data repository (Section DR2). Two NDVI rasters were also generated using GDAL (GDAL/OGR contributors, 2019) for the Toro Basin using 10-m resolution Sentinel-2 (S2) scenes ($NDVI = (band8 - band4)/(band8 + band4)$) from winter (20 July 2017) and summer (11 November 2017). Resulting σ^0 and NDVI rasters were clipped to the Río Toro polygon outline of the active channel and five endmember surfaces in the study area.

5.2. Surface roughness characterization

We do not provide a detailed parameterization of roughness via $Hrms$, L , and/or high-resolution 1-D elevation profile power spectra parameters (Dierking, 1999; Shepard et al., 2001). Such efforts may be appropriate at the plot-scale in relatively homogeneous settings where roughness data are collected at or near the time of SAR measurement (e.g., Weeks et al., 1996; Baghdadi et al., 2008; Aubert et al., 2011), but our studied channel is heterogeneous and large, and our SAR scenes span from 2011 to 2019 (Table DR1). Collecting detailed and spatially continuous soil moisture and roughness data for site-wise parameterization from the exact date and time of each SAR scene is infeasible; although we can assume that over much of the channel the soil moisture is extremely low as the aerially exposed bed is baked to a dry pan in the high-intensity subtropical sunshine (Fig. 4). We are instead interested in studying relative trends in downstream roughness and local channel-bed patchiness within a framework of field observations and geomorphic knowledge. From our theoretical hypotheses in Section 2 we can also determine the utility of various wavelengths and spatial resolutions in measuring channel-bed roughness. We use endmember surfaces to quantitatively assess the hypotheses and use this knowledge to more qualitatively assess trends in channel bed roughness and patchiness, which changes notably along the channel (see photos in Fig. 3). Future work will benefit from detailed site calibration using soil moisture and roughness along with temporally coincident multi-band SAR data, but that is beyond the scope of this study.

5.3. Endmember surfaces

Following the generation of σ^0 SAR rasters we explored the response of the X-, C-, and L-band wavelengths over representative smooth and rough endmember surfaces. First, we chose a collection of four homogeneously rough Quaternary terraces (Fig. 5A; Tofelde et al., 2017). These terraces are flat desert pavements with little sand and the arrangement of gravels and their grain-size distribution is homogeneous, with subtle differences between the terraces related to terrace age (Tofelde et al., 2017). Second, we selected a heterogeneously rough man-made gravel pile, where the pile slopes act as strong scatterers via double-bounce effects (Fig. 5B). For these extreme endmembers (homogeneously rough terraces and heterogeneously rough gravel pile), we took the mean and standard deviation of σ^0 using every pixel from every scene covering the endmember. The mean and propagated standard deviation of each scene individually provided comparable results to combining all scenes.

In a second step, we selected three small sites within the channel area representative of the typical sand and gravel arrangements in the Río Toro (Fig. 6). These included a large area of smooth compacted sand, an area with mixed sand and gravel patches where pebble size was < 0.2 m, and an area with some sand patches and many larger pebbles and boulders. To assess the presence of some seasonal signals in the channel that may relate to soil moisture, we extracted the backscatter values in these three channel endmembers for each scene individually and plotted the mean and standard deviation. These endmembers allow us to assess our initial hypothesis regarding the response of each wavelength to various sand and gravel configurations.

5.4. Downstream trends

We extracted all σ^0 pixels for each sensor and scene separately from within the 115-km polygon outlining the active channel bed to evaluate trends in the signal. All pixels with seasonal NDVI values > 0.15 were masked to remove all but the sparsest vegetation. Furthermore, we masked any pixels that had θ_i values $< 25^\circ$ or $> 50^\circ$, since very high or low angle backscatter returns may be influenced more by look geometry than surface roughness (e.g., Farr, 1993; Baghdadi et al., 2008; Aubert et al., 2011). The remaining σ^0 values were plotted versus upstream distance.

Because of the high data density and variability, we used a 2-D Gaussian Kernel Density Estimate (KDE) to identify the dense and sparse zones of measurement along the channel. Considering the KDE as a 3-D surface with the X and Y horizontal dimensions as distance upstream and σ^0 , respectively, and the Z vertical dimension as the density, we can connect the line of maximum height (density) to extract a trendline that is independent of bin size. Remaining spikiness in the KDE trendline was smoothed using a Savitzky-Golay filter with a second-order polynomial and a window size of 1 km. As a final trendline-smoothing step, the filtered KDE was resampled to an evenly spaced 1-km interval using linear interpolation. In plotting of the smoothed KDE trendlines, we separated scenes into wet (October, November, December, January, February, and March) or dry (April, May, June, July, August, and September) months to examine seasonal signals that may be related to bedload transport and/or soil moisture changes overprinting the roughness signal of interest.

5.5. Sand-gravel patchiness

The previous steps relate to theoretical endmember responses and downstream trends in backscatter intensity. We are also interested in another aspect of geomorphic complexity that may be explored with these SAR data: the changes of inter-pixel variability in SAR backscatter for different geomorphic zones along the channel. That is, the frequency of variation in sand- or gravel-dominated pixels at a given channel location, or the aforementioned patchiness of the channel. Low

patchiness refers to more mixing of sand and gravel, and high patchiness refers to more discrete, contiguous sand- or gravel-dominated patches.

To analyze the patchiness of sand and gravel bedload we remain in X-Y plan-view space to maintain the relation of each pixel to one another. For this, we use the 2-D Discrete Fourier Transform (DFT) to examine the frequency distribution of backscatter. This technique has been widely applied in the geosciences, for example for measuring landscape scaling relationships (e.g., Perron et al., 2008) and DEM artifact identification (e.g., Arrell et al., 2008; Purinton and Bookhagen, 2017). The 2-D DFT transforms a grid of evenly spaced values (σ^0 in our case) from the spatial to the frequency domain. This provides information on the amplitude and periodicity of the values. The power spectrum, magnitude squared of the DFT ($|DFT|^2$), is a measure of the variance of σ^0 with the units of amplitude squared (dB²), and can be plotted against frequency, or wavelength (frequency⁻¹), to evaluate trends in the spatial signal (e.g., Booth et al., 2009).

We refer the reader to the data repository (Section DR3) for a more detailed description, but summarize the steps here. We applied the 2-D DFT to individual 1-km channel clips from each scene to obtain the power spectra. We stacked all coincident 1-km channel clip power spectra to generate large power, frequency value pairs for robust fitting. Using each scene and 1-km channel clip independently led to large scatter in the data collected over 9 years (Table DR1). Stacked clips ignore inter-scene variability, but allow us to confidently assess integrated trends in sand-gravel patchiness. Initial testing demonstrated insufficient resolution (15 m) for the S1 and ALOS2 scenes, as much of the channel upstream of the mountain front was too narrow (Fig. 3C) and contained too few pixels for confident DFT calculation. Therefore, we relied only on the TSX/TDX 5-m scenes. Given the well-mixed, more homogeneous sand and gravel patchiness above ~10 m (Fig. 4), these data are likely at the maximum limit of spatial resolution for this analysis in our study area.

We plotted the stacked arrays of the power against frequency in log space, and fit functional models to the binned data to describe and compare the channel clips. For the 10–18-m wavelengths, we fit a power-law function of the form $f(x) = x^\alpha$, and for the 18–50-m wavelengths we found a better fit using a stretched-exponential function of the form $f(x) = e^{x^\beta}$ (see data repository Section DR3 for details). The exponents (α and β) of these functions describe the distribution of long-wavelength (low-frequency) versus short-wavelength (high-frequency) features in a given fitting range (10–18 or 18–50 m), or the relative development of larger versus smaller areas of similar σ^0 values (i.e., sand- or gravel-dominated patches) in this range.

In this framework, higher negative exponent values (a steeper slope for α or curvature for β) indicate shifting of the power-frequency distribution to longer-wavelength features compared to shorter-wavelength features in the fitting range. In other words, there is relatively less power at shorter wavelengths (higher frequencies), and thus more sand-gravel patchiness developed at longer wavelengths. On the other hand, in a channel reach where the exponent values are lower negative (the slopes are shallower), there are more developed contiguous sand- or gravel-dominated patches at shorter wavelengths. For example, consider two 1-km channel clips: (1) with $\alpha = -6$ and $\beta = -60$; and (2) with $\alpha = -7$ and $\beta = -70$. Channel clip (2) has higher negative exponents (steeper functions) and thus relatively more lower frequency (longer wavelength) sand- or gravel-dominated patches towards the 18-m (for the α fitting range of 10–18 m) and 50-m (for the β fitting range of 18–50 m) wavelengths. Channel clip (1), with relatively lower negative exponents (shallower functions), shows greater patchiness development of higher-frequency (shorter-wavelength) features. Thus, we can use this analysis to say that channel clip (1) has more small sand- or gravel-dominated patches compared to clip (2), which shows relatively more large sand- or gravel-dominated patches within the same frequency ranges.

Table 1
Characteristics of SAR data including smooth-rough thresholds from Peake and Oliver (1971).

Sensor (wavelength)	Pixel size	Number of scenes	Mean ± standard deviation of θ_i over channel (25* cos (θ_i))	Mean ± standard deviation roughness threshold: $\lambda/\sqrt{25*\cos(\theta_i)}$	Mean ± standard deviation roughness threshold: $\lambda/\sqrt{4.4*\cos(\theta_i)}$
TSX/TDX (X-band – 3.1 cm)	5 m	12	36 ± 4°	0.15 ± 0.01 cm	0.87 ± 0.04 cm
S1 (C-band – 5.6 cm)	15 m	15	39 ± 3°	0.29 ± 0.01 cm	1.65 ± 0.08 cm
ALOS2 (L-band – 22.9 cm)	15 m	5	32 ± 3°	1.08 ± 0.04 cm	6.13 ± 0.22 cm

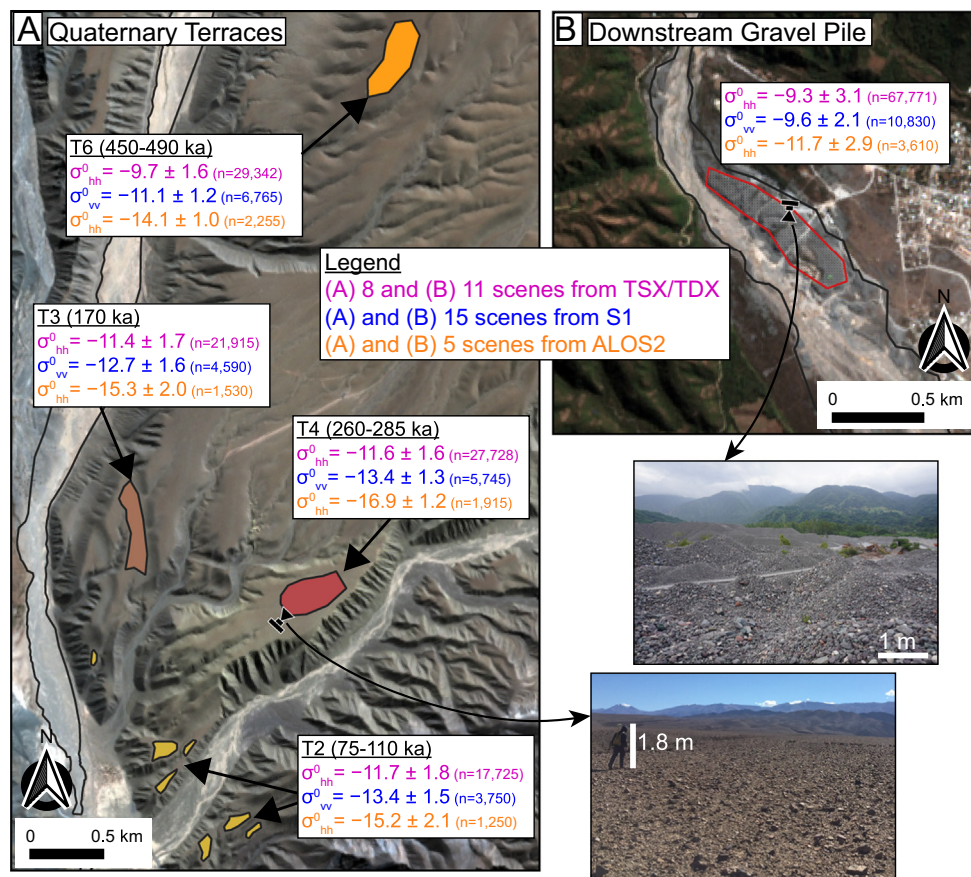


Fig. 5. Differences in X-, C-, and L-band σ^0 (mean \pm standard deviation in dB) from two extreme endmembers (locations are indicated in Fig. 2A). (A) shows the Quaternary terraces with dates from Tofelde et al. (2017) and (B) shows a large man-made gravel pile associated with in-channel gravel extraction. The locations of inset field photos are given by the camera icon. The color scheme given in the legend is pink for TSX/TDX, blue for S1, and orange for ALOS2. Not all 12 TSX/TDX (Table DR1) scenes had coverage of each location, as indicated by the number of scenes in the legend. The river (black outline) always flows approximately north to south. Inset pictures taken from each area during fieldwork. Basemap imagery is the S2 scene used in Fig. 1. We note that the terrace polygons are not identical to Tofelde et al. (2017). We used custom clips that were roughly the same size (n is the total number of pixels for each sensor from all scenes in each polygon) and only from flat terrace-top surfaces away from frequent gullies, small valleys, and side-slopes, which may be unduly influenced by look-geometry of the satellite sensor. (For interpretation of the references to color in this figure legend, the reader is referred to the web version of this article.)

6. Results

6.1. Endmember surfaces

A dataset summary in Table 1 shows that the Peake and Oliver (1971) mean smoothness thresholds occur at 0.15, 0.29, and 1.08 cm, and the mean roughness thresholds at 0.87, 1.65, and 6.13 cm for the X-band TSX/TDX, C-band S1, and L-band ALOS2 scenes, respectively. As discussed in Section 2, where the average height of roughness elements is below the smooth threshold, we expect low σ^0 as the signal is reflected away from the sensor, and where the surface is above the rough threshold we expect high σ^0 . The range between these transitional values indicates the range of expected responses, particularly on mixed smooth- and rough-surfaces.

The extreme endmember clips from the Toro Basin and the resulting average and standard deviation σ^0 co-polarized values are shown in Fig. 5. As expected from wavelength considerations, the ALOS2 data always have a lower mean backscatter signal, since the surfaces appear more smooth. It follows that the TSX/TDX data have the highest mean values. Through a combination of gravel and boulder elements and double-bounce effects on the slopes of the pile, the gravel pile has the greatest mean σ^0 for each sensor, with a range of difference in mean values to the terraces of 0.4–2.4, 1.5–3.8, and 2.4–5.2 dB for X-, C-, and L-band, respectively, which indicates the greater sensitivity range of ALOS2 L-band. Importantly, we note the tighter σ^0 (lower standard deviation) over homogeneously rough surfaces, like the terraces (maximum 2.1 dB for ALOS2 on the youngest terrace T2, but typically 1–2 dB), versus for more heterogeneously rough surfaces, like the gravel pile (maximum 3.1 dB for TSX/TDX, and all > 2 dB).

Moving from the extreme examples to the more typical sand- and gravel-mixed Río Toro channel bed, example clip results are presented in Fig. 6. Locations of these three sites are indicated in the caption with

reference to Fig. 3. These plots are now separated by date, and the results from Fig. 5 are also displayed for reference.

Regarding a seasonal or time-series signal (possibly related to soil moisture or bedload transport, since all three sites have little to no vegetation), the standard deviation envelopes instead show the high variability in SAR backscatter measurements. The envelopes maintain a fairly consistent range of 2–4 dB, but they show significant scene-to-scene shifts, even in the far upstream smooth sand site, where little to no change is expected in the time frame of scene collection. This indicates that sensor-related noise in measurement is an important caveat to measuring roughness variation between scenes (especially regarding small seasonal changes at a location).

Despite this caveat, clear differences in σ^0 are apparent based on the clast arrangement and radar wavelength. In all three bands there is a large separation between the smooth sandy surface in the far upstream Río Toro and the more pebbly and bouldery clips, with the standard deviation envelopes showing no overlap and a similar mean difference of 4.8–5.1 dB to the pebbly surface. Another key result from this analysis can be seen in the ALOS2 L-band sensitivity to the pebbly versus bouldery surfaces, with a mean separation of 2.2 dB and only slight envelope overlap (Fig. 6A). This is expected given the high L-band threshold for saturation of 6.13 cm. On the other hand, both the TSX/TDX X-band and S1 C-band show only a 0.7 dB separation with high overlap in the envelope. Thus, the X- and C-band wavelengths become saturated with the inclusion of even smaller pebble elements, and differences in backscatter for these sensors will primarily reflect sand-patch contribution.

6.2. Downstream trends

With a detailed understanding of expected σ^0 response over end-members, we now examine the continuous signal along the entire

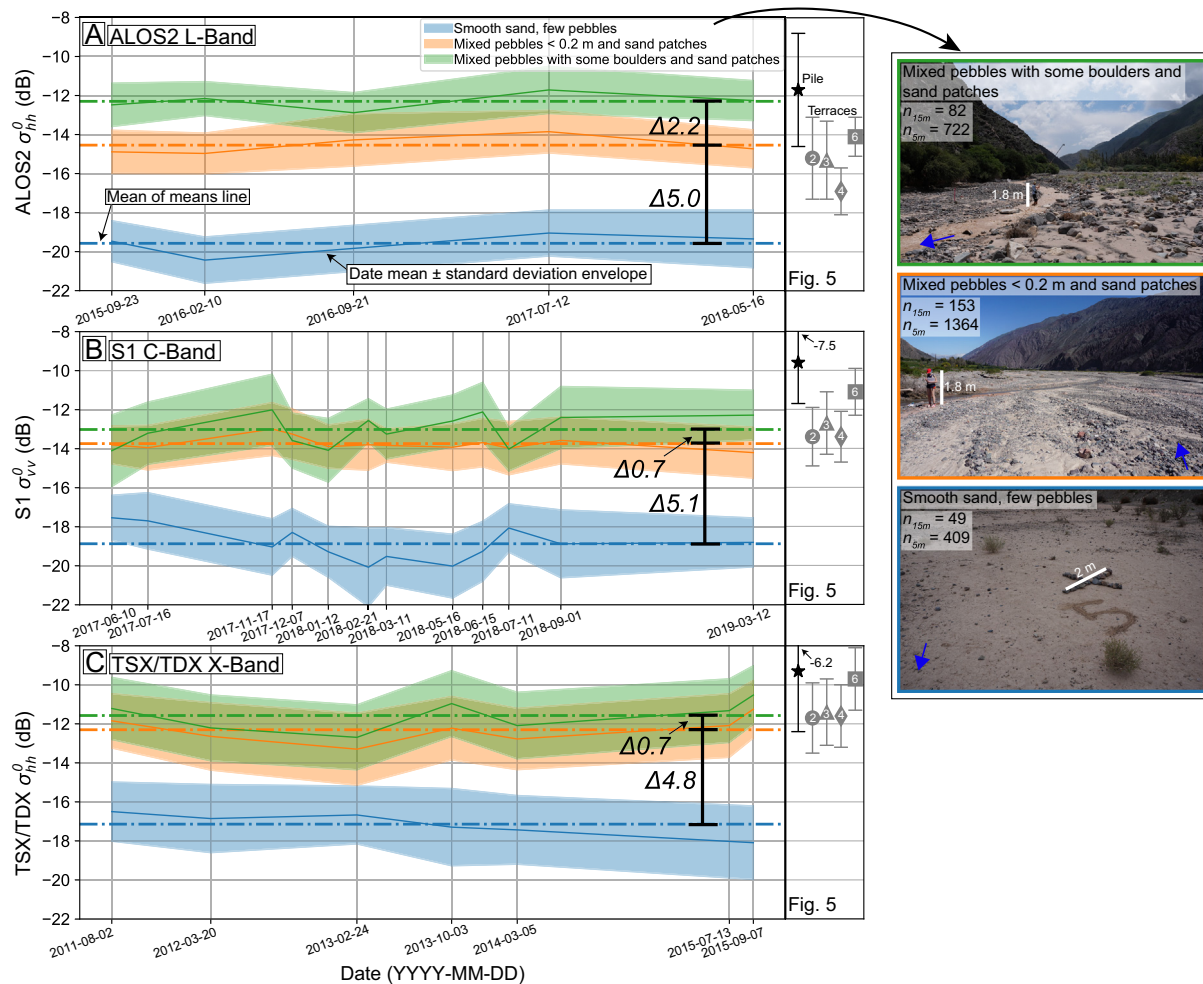


Fig. 6. Differences in X-, C-, and L-band σ^0 from typical channel endmembers. (A) shows the ALOS2 scene mean and standard deviation envelope (solid line and transparent polygon) and mean line (dashed line, taken as the mean of the mean date-wise values for each site). (B) shows S1 and (C) shows TSX/TDX. In the inset photos the sandy (blue), mixed pebble (orange), and bouldery (green) areas are from photo locations P8, P6, and P5 in Fig. 3, respectively, and the blue arrow indicates flow direction. The inset n_{15m} and n_{5m} in the field photos are the total number of pixels contained in each area for the 15-m ALOS2/S1 and 5-m TSX/TDX scenes, respectively. The mean \pm standard deviation for the extreme endmembers in Fig. 5 (integrating all available scene dates with coverage) are also shown on the right side of each subplot for comparison. Note that not all dates were used for S1 as some scenes were collected from within one week of each other and their inclusion caused clutter and did not change the interpretation. Also, some TSX/TDX scenes did not cover each (or any) of the three sites (see smaller SAR footprint in Fig. 2A). (For interpretation of the references to color in this figure legend, the reader is referred to the web version of this article.)

channel reach. Fig. 7 contains an example analysis from one S1 scene as discussed in the Methods. (Fig. DR1 in the data repository contains examples using TSX/TDX and ALOS2 scenes.) There is an increase in NDVI values within the channel downstream of the mountain front at (1) and in some low-slope reaches upstream of the knickzone at (4), with the mean 1-km-binned NDVI (Fig. 3B) sometimes exceeding the 0.15 threshold for masking. However, many pixels remain as indicated by the counts in Fig. 7C. Fig. 7A shows the spikiness of the overall trend when using a 500-m binning approach. This high-frequency component is removed and we are able to extract a smooth trendline from the profile using the KDE in Fig. 7B. The sparse measurements between (4) and (5) are indicated by the counts per 500-m bin in Fig. 7C. Here, in the region of the Quaternary terraces, channel slopes are low and the river narrows (Fig. 3C) and meanders at times in a wide floodplain.

KDE trendline extraction was repeated for every sensor and date. This was done for the co- and cross-polarized bands (for S1 and ALOS2), and, as expected from the theoretical consideration in Section 2, the cross-polarized results were similar only lower in magnitude, and we thus only present the co-polarized results here. The trendline for each date was then plotted, and colored by wet or dry season to further check for seasonality (i.e., moisture).

Initial results for TSX/TDX indicated many extreme outliers in the trendlines, so these results are shown in the data repository Fig. DR2. This is likely due to the higher spatial resolution (5 m), greater diffuse reflections at the shorter wavelength for this sensor, and possible strong interactions (more diffuse reflection) with turbid water surfaces (see P2 in Fig. 3). Also, sensor noise and processing artifacts (e.g., from our use of the 30-m SRTM DEM for terrain correction in SNAP, rather than a higher resolution DEM to match the TSX/TDX data), may have introduced additional errors. Therefore, we eliminated these sections of the scenes from analysis, with the final area considered from each TSX/TDX scene displayed in the cleaned trendlines of Fig. DR3. From these trendlines, we do note some similar basin-scale downstream trends between the TSX/TDX scenes and the S1 data presented in Fig. 8.

For the S1 trendlines in Fig. 8A, we note that there is no clear seasonal difference between the wet- and dry-season scenes, which lends evidence to the dominance of roughness differences over moisture differences in SAR backscatter response for aerially exposed sand- and gravel-bed channels. Furthermore, there is no difference when separating the scenes into ascending or descending passes, and we can thus neglect look direction as a factor in amplitude differences. As expected from the scene-to-scene variability in Fig. 6, the spread in trendlines

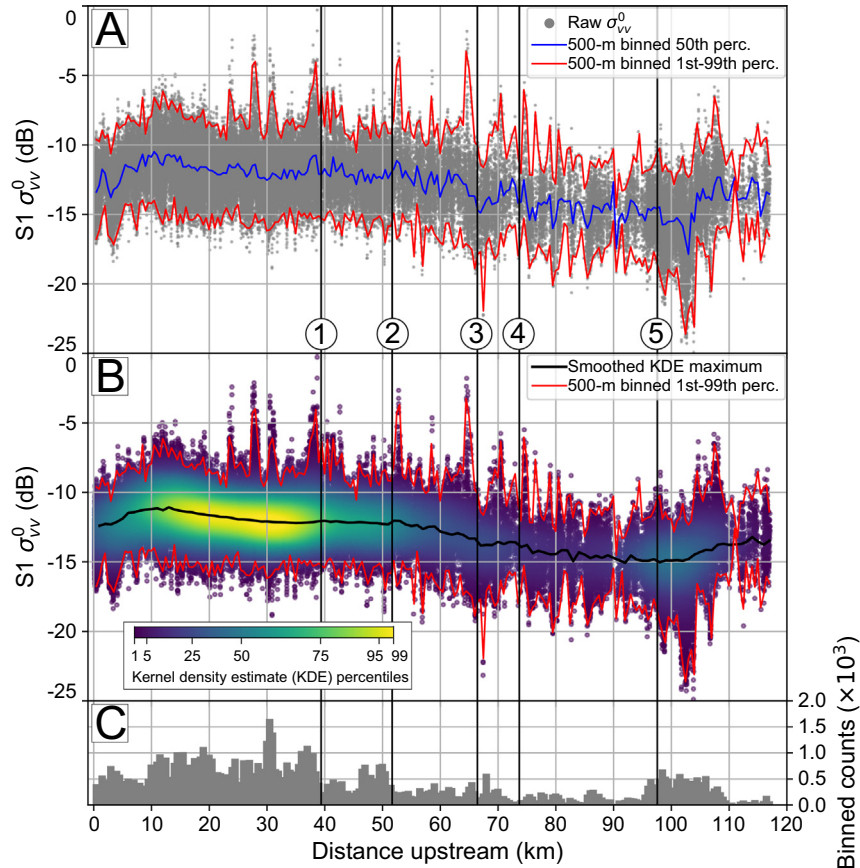


Fig. 7. Example point cloud and trendline extraction for one S1 scene (20180901). The tectono-geomorphic transitions (1–5) correspond to Fig. 2B. (A) is the raw point cloud (masked for NDVI > 0.15), with the 50th and 1st–99th percentile lines (binned in 500-m steps) plotted over it. To remove the spikiness and get an average trendline we go to (B), where the median line is replaced with the smoothed 2-D KDE maximum. (C) shows the 15-m SAR pixel counts per 500-m bin. See Fig. DR1 in the repository for examples using TSX/TDX and ALOS2 scenes.

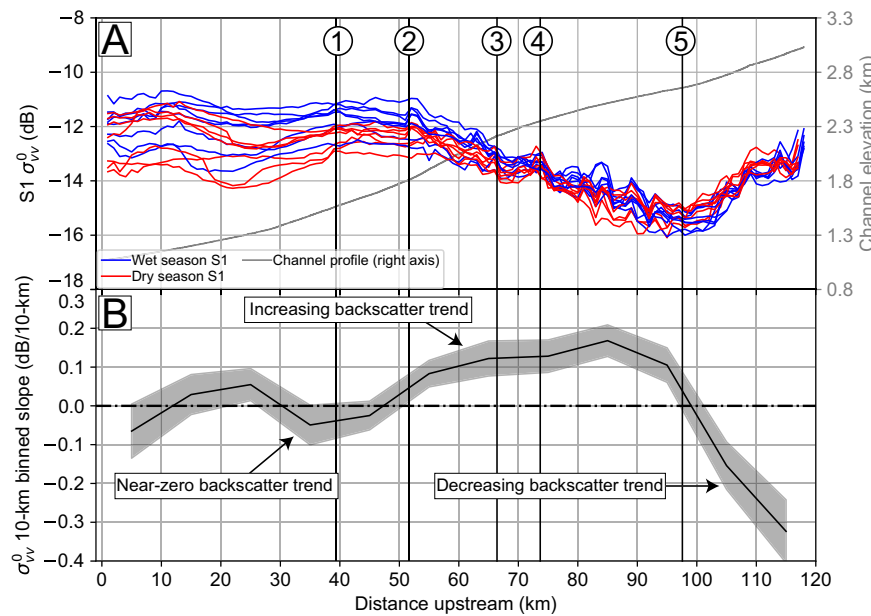


Fig. 8. Smoothed KDE σ_{vv}^0 trendlines for S1 C-band. (A) shows each trendline for the 15 scenes, separated by wet (blue) and dry (red) months, with the channel elevation profile from Fig. 3A included on the right axis for reference and tectono-geomorphic transitions (1–5) corresponding to Fig. 2B. (B) shows the mean and standard deviation trendline slope in 10-km bins, highlighting basin-scale trends in the C-band results. (For interpretation of the references to color in this figure legend, the reader is referred to the web version of this article.)

cover \sim 1–3 dB at a given upstream distance. This is partially caused by sensor noise-related variability, but we do note that the largest spreads occur downstream of the mountain front at (1), indicating possible variable water-surface interactions with different discharges at each date (at times covering a large portion of the channel bed).

Given this spread, we are hesitant to present an integrated, or average, trendline. Instead, we take note of the similar tendency (shape) of each trendline (increasing or decreasing) and use this to extract the average and standard deviation of σ^0 trendline slopes in 10-

km bins in Fig. 8B. We experimented with 1-, 2-, 5-, and 10-km binning distances, and found the 10-km bins to most clearly demonstrate the basin-scale trends of interest from S1. Extending this analysis to the L-band ALOS2 data in Fig. 9 shows more detailed results. Again, we see little seasonal signal in the L-band, with the backscatter spread at one location instead caused by ALOS2 sensor-related noise and possible soil moisture or water-surface interactions downstream of the mountain front. However, such interactions should cause differences in the shape of the backscatter trendlines for S1 and ALOS2, caused by variable

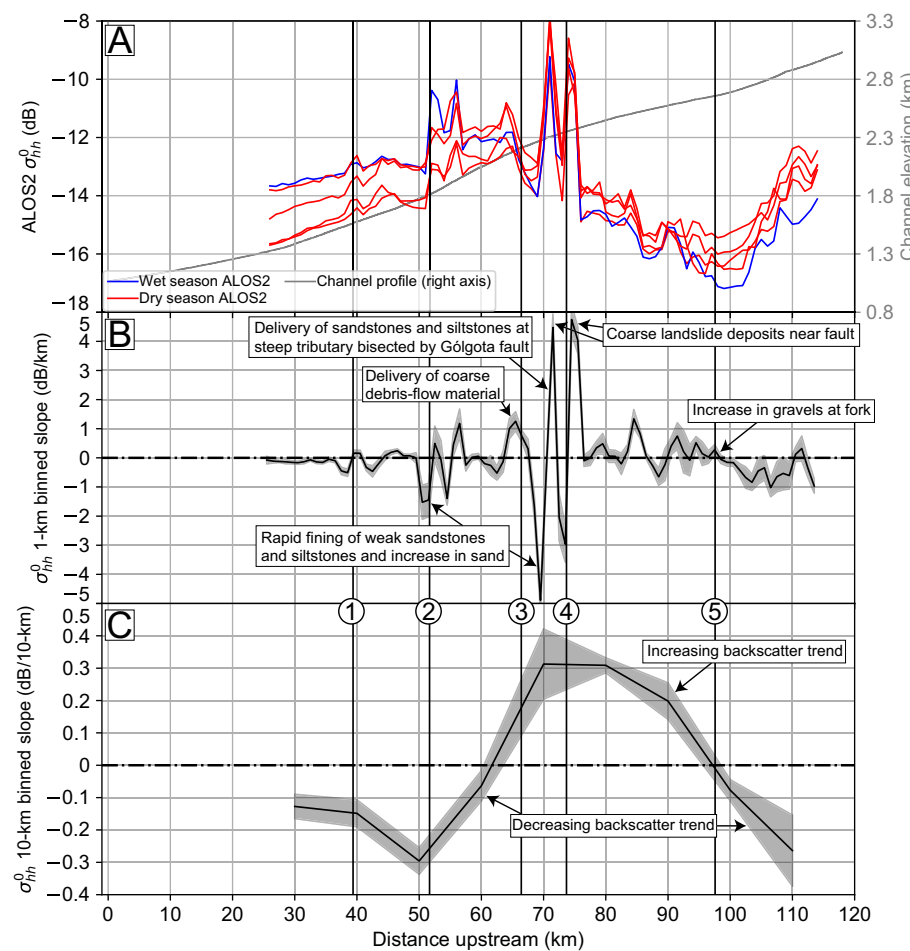


Fig. 9. Smoothed KDE σ_{hh}^0 trendlines for ALOS2 L-band. (A) shows each trendline for the 5 scenes, separated by wet (blue) and dry (red) months, with the channel elevation profile from Fig. 3A included on the right axis for reference and tectono-geomorphic transitions (1–5) corresponding to Fig. 2B. (B) shows the mean and standard deviation trendline slope in 1-km bins, highlighting fine-scale trends (note text boxes) in the L-band results, and (C) shows the slope in 10-km bins, which is similar to the C-band trends shown in Fig. 8B. (For interpretation of the references to color in this figure legend, the reader is referred to the web version of this article.)

moisture or water-surface area at a given upstream distance, rather than a scalar shift in values at one location as observed in the C- and L-band trendlines. Thus, we attribute this variability primarily to sensor noise.

The L-band data contain clear increasing and decreasing trends in local channel segments when using a finer 1-km slope binning (Fig. 9B), and a similar basin-scale trend to the S1 data using the same 10-km bin length (Fig. 9C). Interpretation of these trends, their differences between sensor, and their geomorphic implications are provided in greater detail in the Discussion section.

6.3. Sand-gravel patchiness

The high variability demonstrated with the spiky median line and 1st–99th percentile envelope in Fig. 7A indicates local geomorphic complexity of the channel bedload beyond the downstream trends. Certain localized spikes can be connected to notable features in the field; for instance, the large positive excursions between 25- and 40-km upstream in Fig. 7B relate to the man-made gravel piles in this reach noted in Purinton and Bookhagen (2018) and shown in Fig. 5B. Some local complexity is also captured in the fine-scale trendline slope analysis for L-band SAR (Fig. 9B), but we can go beyond this using the frequency analysis and higher resolution TSX/TDX data to examine the sand-gravel patchiness. Importantly, since the TSX/TDX X-band data has a low roughness threshold of 0.87 cm (Table 1), the frequency analysis is most sensitive to pixels ($5 \times 5 = 25\text{-m}^2$ pixel area) that contain predominantly smooth sand.

Fig. 10 contains an example of our 2-D DFT frequency analysis for the TSX/TDX data. The data repository Fig. DR4 shows examples of the preprocessing of these 1-km clips to rectangular, void-free grids for DFT

analysis. Only the channel sections of each scene displayed in the noise-cleaned trendlines of data repository Fig. DR3 were used for this analysis. Combined with stacking, the high spatial resolution of the TSX/TDX data allowed fitting of power-law and exponential functions to 56 and 51 stacked 1-km clips, respectively, out of a possible 116 clips (1-km each along the ~116-km channel length) with TSX/TDX coverage. The remaining clips were either too narrow (< 8 pixels, or 40 m), contained too many void-spaces (> 40%), or produced poor power-law or exponential fits (see data repository Section DR3 for details of DFT analysis).

Although only a small range of frequency bins were fit by the short-wavelength power-law with fixed x_{min} at 18 m (see data repository Fig. DR5), this range (10–18 m) accounted for ~74% of the unbinned 10–50-m power spectrum values. The exponential fits with variable x_{min} between 30 and 50 m, and fixed x_{max} at 18 m, covered ~24% of remaining values. Thus, the combined two-function model was able to fit ~98% of the raw data.

From the stacked 1-km TSX/TDX channel clips, the two exponents (α and β) are plotted against channel distance in Fig. 11. Sand-gravel patchiness developed predominantly at lower or higher frequencies is related mostly to contiguous sand patches in each 25-m² pixel and the arrangement, or clustering, of those pixels with similar σ^0 values in space. A higher negative exponent (steeper slopes, relatively less power at shorter wavelengths) corresponds to more sand patches developed at longer wavelengths. Conversely, a lower negative exponent (shallow slopes, relatively more power at shorter wavelengths) corresponds to more sand patches developed as shorter wavelengths. We interpret these downstream to upstream results in the proceeding discussion.

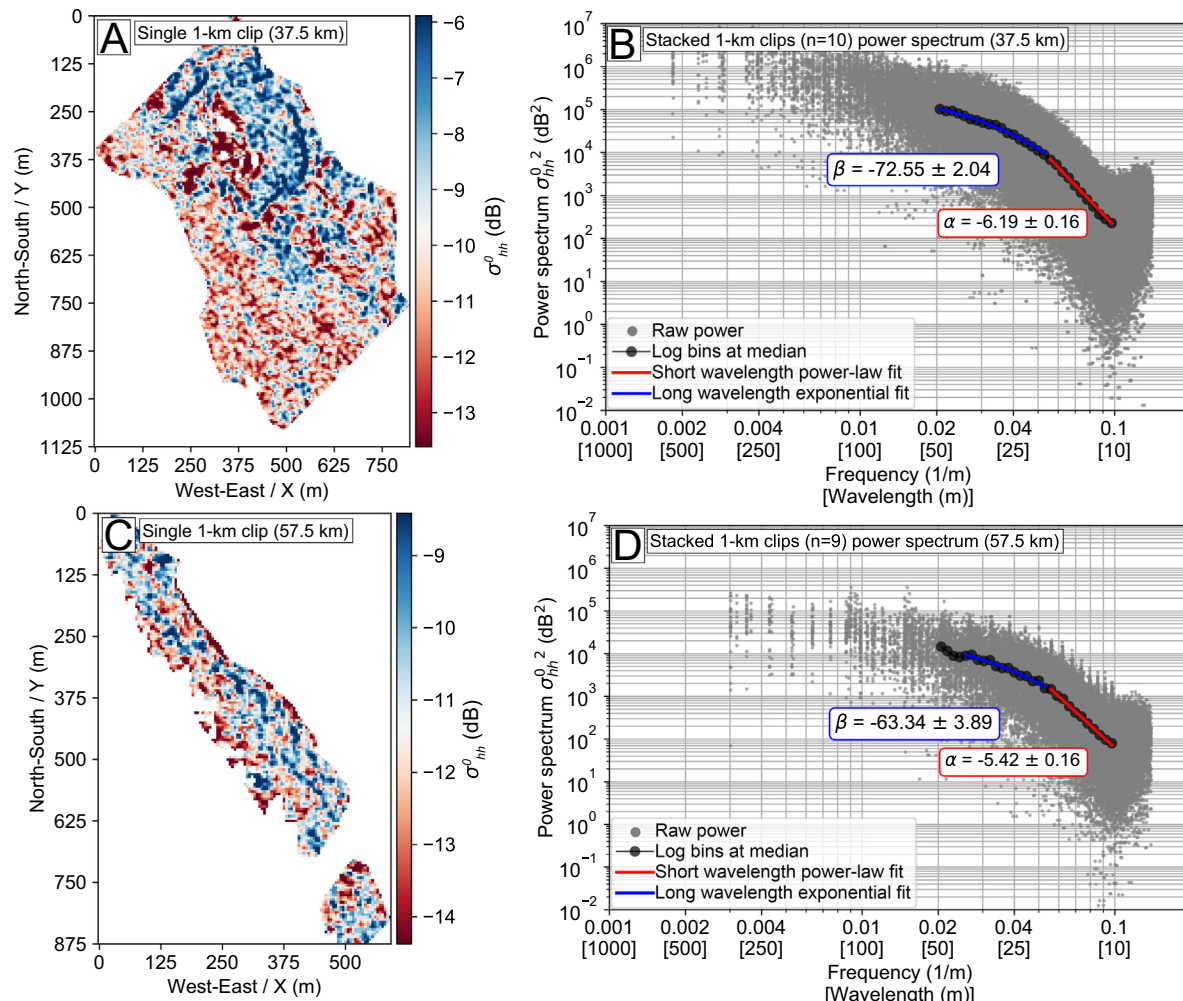


Fig. 10. Example 1-km channel clips and 2-D DFT analysis from one TSX/TDX 5-m resolution scene (20150928) from (A) 37.5-km and (C) 57.5-km upstream, with σ_{hh}^0 color scale going from the 5th–95th percentile of all values in the clip. Each clip undergoes preprocessing to create a void-free rectangular grid (see data repository Section DR3 and Fig. DR4). The power spectrum in (B) shows all power-frequency raw values from 10 stacked scenes for the 1-km channel clip shown in (A), and the spectrum in (D) shows the same but for only nine available scenes covering the clip in (C). The stacking leads to a dense point cloud that can be binned and fit by one power-law (α) and one stretched-exponential (β) function. The higher negative values for α and β from the further downstream clip (B) indicate relatively (compared to the further upstream clip) greater sand-gravel patchiness developed at longer wavelengths and relatively less higher-frequency (shorter-wavelength) patches. (For interpretation of the references to color in this figure legend, the reader is referred to the web version of this article.)

7. Discussion

Our results demonstrate a novel use of SAR backscatter amplitude measurements in a dynamic, high-mountain fluvial environment. The use of multiple wavelengths and resolutions show important differences and limitations of the sensors for channel-bedload measurement applications. In this discussion, we describe these differences in relation to other studies of surface roughness using SAR, highlight geomorphic interpretation of our data, and indicate the potential uses of the method in braided alluvial rivers. We also discuss limitations of the sensors and method and possible avenues for further research.

7.1. Range in backscatter for endmembers

The channel endmembers in Fig. 6 show a range in mean X-, C-, and L-band σ^0 of 5.5, 5.8, and 7.2 dB, respectively, going from smooth sand surfaces to mixed sand, pebbles, and boulder surfaces. Baghdadi et al. (2008) found a similar range of X-, C-, and L-band of 4–5.5, 4, and 8 dB, respectively, on plowed agricultural fields with soil *Hrms* values of ~0.5–3.5 cm. These relationships between *Hrms* and σ^0 are non linear and typically reach a rapid plateau at *Hrms* values of ~1, ~1.5, and

~2 cm for X-, C-, and L-band, respectively, beyond which the soil surface is radar saturated and increases in roughness have little effect on σ^0 (Baghdadi et al., 2008, 2018). The exact range of σ^0 and the plateau (saturation) values have varied slightly in different agricultural studies (e.g., Aubert et al., 2011; Gorrab et al., 2015; Bousbih et al., 2017), but are in general agreement.

Radar roughness studies from plowed agricultural soils with mixed sand, silt, and clay content are less applicable to our fluvial setting with mixed compacted sand and gravels, where little quantitative research on backscatter response has been done. To our knowledge, the only study of SAR bed-roughness in a hydrological sense is from Sadeh et al. (2018). Here, Manning's *n* (the hydrological roughness of a surface) was shown to correlate well with X-band backscatter. They found a ~4-dB range over rock types from desert pavement to stony limestone and a ~1.5-dB range over *Hrms* heights from 0.7–1.7 cm.

Much non-agricultural research has focused on morphological differences of dry desert alluvial fans, which show backscatter differences as a smooth desert pavement forms over millennial time-scales (e.g., Farr and Chadwick, 1996; Kierein-Young, 1997; Hetz et al., 2016). Such differences in σ^0 from the different Quaternary terraces in Fig. 5A may be related to terrace age (Tofelde et al., 2017) and morphological

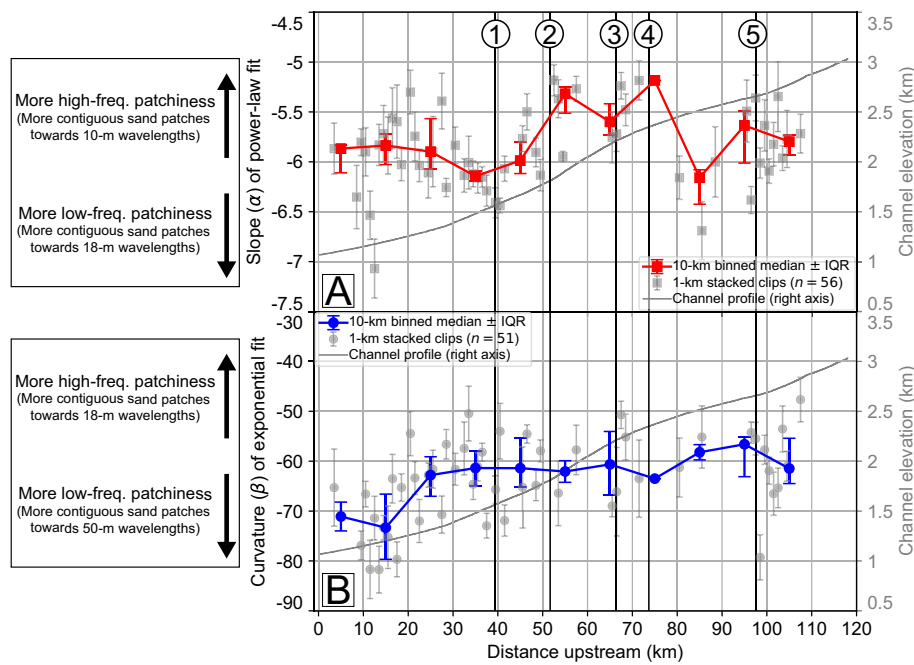


Fig. 11. Downstream trends in (A) α and (B) β of the power-law and stretched-exponential fits, respectively, for the stacked 1-km channel clips from the 5-m TSX/TDX scenes. To provide spatial context, each plot includes the channel elevation profile (gray line) on the right axis (see Fig. 3A), where the tectono-geomorphic transitions (1–5) correspond to Fig. 2B. Each stacked clip is shown with gray symbols and 1-standard deviation error bars. To highlight the overall trends, these exponents are aggregated in 10-km bins at the median value with per-bin Interquartile Range (IQR) error bars. More negative values correspond to relatively more sand-dominated patches developed towards longer wavelengths (lower frequencies), whereas lower negative values correspond to relatively more sand-dominated patches developed towards shorter wavelengths (higher frequencies), in the 10–18-m or 18–50-m wavelength range for α and β , respectively.

differences, whereby weathering processes reduce clast size, thus smoothing the surface over time (Hetz et al., 2016). The tighter spread (lower standard deviation) on these terraces demonstrates the effect of a spatially homogeneous roughness, with similar rock sizes and rock spacing over a large area (see inset photo in Fig. 5A).

Deroine et al. (1997) measured properties of loose rocks in desert test plots and found log scaling over a ~16-dB range in C-band σ^0 , going from silt- to rock-dominated surfaces with a maximum rock-height range of ~0.5–15 cm (with a plateau in σ^0 beginning at ~4 cm). As discussed in Section 5.2, we do not have the detailed site calibration data to provide metrics like rock-height range, however, when considering the full range in S1 C-band σ^0 from the approximate minimum of the standard deviation envelope of the sandy area (~21 dB) to the maximum standard deviation spread of the gravel pile (~7.5 dB) (see Fig. 6B), we find a similar range of 13.5 dB.

Such results indicate the ability of distributed roughness elements (i.e., gravels on top of a sandy surface) to modulate backscatter intensity beyond expected saturation plateaus, as each $5 \times 5\text{-m}$ (25-m^2) or $15 \times 15\text{-m}$ (225-m^2) pixel SAR measurement may contain a mixture of both smooth and rough patches. The greater difference of L-band to the pebbly and bouldery surfaces in Fig. 6A, also shows how longer wavelength SAR has a higher saturation plateau and may be more useful for assessing differences in downstream grain size, whereas C-band, and especially X-band, is less sensitive to changes beyond sand-gravel transitions.

7.2. Backscatter trends and geomorphic implications

Our assessment of expected (from previous work) and observed (from endmembers) backscatter response allows us to interpret downstream trends along the Río Toro. Although we lack extensive calibration data for a quantitative discussion, detailed knowledge of the study area gained through fieldwork and extensive channel-bed cross-section photo surveys (Purinton and Bookhagen, 2019a) allows us to make consistent, qualitative statements about observed trends.

S1 C-band and ALOS2 L-band 10-km binned trendline slope results in Figs. 8B and 9C, respectively, show a common feature of negative trends upstream of the channel fork at (5) switching to positive trends downstream. Upstream of this fork, large quantities of sand are sourced from the loose slopes of the large Quaternary terraces (Fig. 5A),

whereas downstream of the fork there are increases in gravels. Thus, both datasets capture the approximate sand-gravel transition in the Río Toro.

For S1 C-band (Fig. 8), increasing σ^0 (positive slopes) continues from the upstream fork at (5) all the way to the tributary confluence at (2). Based on endmember considerations for S1 data, we interpret these trends to be related to the reduction of contiguous sand patches via mixing of gravel elements. The C-band σ^0 is saturated at 1.65 cm (Table 1), so there may be some response to modulation of grain size downstream, but decreased sand is most important. The confluence with the large tributary at (2) presents another change point for the S1 C-band as large amounts of sand are again introduced by weathered Cretaceous siltstones and sandstones sourced from this tributary basin that quickly degrade to sand. Downstream of (2) the trends become more constant with the 10-km binned slope near zero. Remaining trendline variability downstream of (2) is difficult to interpret given the inherent noise in these individual SAR scenes. Slight modification may be caused by additional small tributary links delivering sand and/or gravels to the main channel, anthropogenic tampering via gravel mining (Purinton and Bookhagen, 2018), bed armoring (see P1 in Fig. 3), and river-water surface interactions (see P2 in Fig. 3), but this is difficult to say without detailed calibration data (discharge, soil moisture, grain-size metrics) for each scene.

Regarding ALOS2 L-band, the 10-km binned trendline slope (Fig. 9C) is similar to C-band, responding to changes in sand fraction. There is a decreasing trend in the sandy reach upstream of (5), switching to an overall increasing trend downstream into the gorge via reduction in sand. A key difference to the C-band trend is apparent at ~65-km upstream in the gorge, where the L-band increasing trend in the 10-km binned slope switches back to decreasing. This is likely related to the fining of gravels to below the higher 6.13-cm L-band roughness threshold (Table 1). The greater grain-size variability captured by the longer wavelength L-band SAR becomes apparent in the 1-km binned results (Fig. 9B). This variability is linked to a combination of sand-fraction and gravel-size changes, corresponding to tectono-geomorphic transitions and tributary inputs, as indicated with some text boxes and arrows in Fig. 9B.

To summarize the observed L-band 1-km binned trends based on field knowledge: Downstream of the fork at (5) but upstream of the Gólgota Fault at (4) there are frequent, small changes in grain size

where fans from terraces, paleolakes, and paleolandslide deposits meet the channel bed. Just upstream of the fault at (4) are a number of coarse paleolandslide deposits, likely associated with Quaternary activity of the Gólgota Fault (Marrett et al., 1994), which lead to spikes in backscatter intensity. The double-spiked feature at ~70–75-km upstream is caused by this coarse material delivered from the steep hanging-wall bedrock walls directly to the channel bed. A dip between the two spikes in Fig. 9A causes a flip from increasing to decreasing and back to increasing backscatter in Fig. 9B. This dip may be partially related to slightly finer gravels and increased sand in this ~1–2-km channel reach, however, we note that this is a locally narrow channel section with few 15-m pixels available for interpretation (see the data repository Fig. DR1 for the 500-m binned pixel count). Just downstream of the double spike at ~70-km the Río Toro crosses a junction with a small, steep catchment bisected by the Gólgota Fault. Abundant, highly erodible Miocene sandstones and siltstones exposed in this sub-catchment deliver a large amount of sand to the Río Toro, leading to a rapid decrease in backscatter intensity. (This response to tributary sand delivery is repeated again at (2) with a rapid decrease in backscatter.) The zone of finer grain size and low backscatter intensity around 70-km upstream is quickly interrupted by the confluence with a coarse debris-flow dominated fan at (3), which again increases the grain size and backscatter intensity. Further fluctuations downstream of (3) in the steep bedrock gorge are related to frequent small landslides delivering a wide grain-size distribution to the channel.

As noted in the Methods, the assessment of sand-gravel patchiness via power-law and exponential model fitting to backscatter power spectra was only possible using our 5-m TSX/TDX data. These X-band data primarily reflect the contribution of smooth sand patches, as even small gravels will rapidly saturate the signal (roughness threshold of 0.87 cm, see Table 1). The high variability from the stacked 1-km channel clip exponents, shown in Fig. 11 by the gray symbols, is expected given the dynamic channel. Sand and gravel patches shift often between seasons and over years, and the X-band 5-m data are sensitive to even small changes. Integrating TSX/TDX scenes collected over 5 years (including both real changes in grain size and inherent noise in the individual scenes) in the stacked 1-km clips further contributes to the large range of α and β in Fig. 11.

Despite the large spread in the exponent values and sometimes sparse data availability (e.g., narrow sections of the channel from 75 to 95-km upstream), we can make some tentative interpretations of the frequency results as they relate to geomorphic understanding. For the shorter-wavelength (10–18 m) power-law fits (Fig. 11A), α increases from upstream of the fault at (4) into the steeper bedrock gorge. This implies a decrease in lower-frequency contiguous sand patches and a relative increase in more high-frequency sand patches. Thus, in the steeper, more geomorphically active gorge, there are less large contiguous sand patches with more frequent changes in the grain-size distribution over shorter distances, matching expectations from field observations. Upstream of the gorge there are more large contiguous sand-dominated patches given the lower channel slope, delivery of terrace-derived sand, and arid conditions leading to stability of sand patches over longer time periods compared to the gorge. Downstream of the tributary confluence at (2) there is a shift to higher negative α values, because there is the influx of sand from the weathered sandstones and siltstones, and the channel also widens significantly in this reach (Fig. 3C) creating accommodation space for stable, large sand patches. Downstream of the mountain front at (1), α clusters tightly in the 30–40-km reach, where anthropogenic modification (gravel mining; Purinton and Bookhagen, 2018) and high bedload transport creates more constant patchiness at the 10–18-m wavelength scale. Sand patchiness scatters downstream of 30 km, where there is a diverse mix of sand and gravel arrangements in the low-slope, wide-channel foreland (Fig. 3C), where frequent higher flows (see P2 in Fig. 3) cause rearrangement of patches.

For the long-wavelength (18–50 m) stretched-exponential fits

(Fig. 11B), β has a slight overall decreasing downstream trend. This implies increasing low-frequency (towards 50-m wavelength) contiguous sand patches as we travel downstream, but there is significant scatter in the data. This scatter is expected from field knowledge and the photos in Fig. 4, which show diverse, mixed grain-size arrangements at larger scales, and fewer elongated gravel- or sand-dominated bars. The slightly pronounced trend towards relatively more large sand patches in the 20–30-km and 10–20-km bins may indicate that in this longer-wavelength (18–50-m) range, the presence of large contiguous sand patches increases in the foreland, but this is difficult to determine without detailed site parameterization data in the form of roughness profiles.

7.3. Caveats and application of the method

Throughout our analysis, we have mentioned the river-water surface in the channel, which may modulate the roughness signal (e.g., Hwang and Fois, 2015; Uddin et al., 2019). Upstream of the mountain front the width of the active channel is limited to $< \sim 10$ m (Fig. 4), so there is limited effect of the water surface in the typically > 100 -m wide channel bed. Downstream of the mountain front, the active channel width can locally exceed ~ 50 m (P2 in Fig. 3). However, in this downstream region the channel bed is typically > 200 -m wide, in places exceeding 800 m (Fig. 3C). Thus, these water pixels should have a limited overall effect on the integrated signal of many pixels over months to years of scene collection. Using scenes from many dates (including during the lower discharge dry season), insures that most of the channel bed is exposed to direct SAR measurement of sand and gravels. Nevertheless, researchers interested in applying this method should be aware of the complicating effect of water surfaces in channels that maintain higher flow conditions, submerging the bedload of interest.

In highly active alluvial channels in steep, high-mountain environments with mixed sand and gravel grain-size distributions, the variability in sand- or gravel-dominated patches often occurs over short (< 50 m) distances. Thus, our TSX/TDX data are likely near the limit of sand-gravel patchiness measurements, with lower-resolution data (e.g., 15 m) integrating signals over scales at which the channel-bed material is more homogeneous and well-mixed. Higher-resolution TSX/TDX data are possible from the spotlight sensing mode (e.g., Aubert et al., 2011) or with lower multilooking, however, there is a trade off between the signal-to-noise ratio as resolution or multilooking is decreased. Channel-bed patchiness via the power spectrum approach is likely limited to only high-resolution SAR sensors, but it is nevertheless a novel use of DFT analysis for SAR amplitude data, extendable to other surfaces of interest (e.g., agricultural fields).

Mapping full grain-size distributions is challenging from SAR data alone. Longer-wavelength P-band ($\lambda = 68$ cm) measurements have shown even greater ranges in roughness sensitivity with some potential for mapping grain-size distributions using combinations of L-, and P-band (e.g., Campbell and Shepard, 1996; Campbell, 2001), but these sensors are rare. L-band data alone are shown here to be sensitive to some changes in grain-size, but further work involving detailed site parameterization along with temporally coincident SAR measurements are necessary to move this analysis into a more quantitative framework.

Thus, for the time being, SAR amplitude measurements over alluvial sand- and gravel-bed rivers in high-mountain environments are limited to measuring the gravel-sand transition zones with some accuracy (i.e., changes in backscatter trend from positive to negative slopes as sand increases), and to determine relative changes in grain-size using longer wavelength SAR. The gravel-sand transition is of great interest in understanding mechanisms of downstream fining via processes of abrasion or selective transport (Lamb and Venditti, 2016; Dingle et al., 2017), and the proposed methods could be applied at large scales using river outlines extracted by manual digitization on freely available imagery (Fisher et al., 2013).

8. Conclusions

SAR amplitude is a useful, weather independent, remote-sensing tool for measuring surface roughness from space. Previous research has focused primarily on applications to water surfaces, agricultural fields, or dry desert alluvial fans. Here, we have presented a novel use of SAR amplitude data applied to high-mountain alluvial channel bedload measurements. Through presentation of theory and hypothetical backscatter responses, testing on endmember surfaces, and careful trendline consideration, we demonstrated the limits of various radar wavelengths for this analysis. The described method is not able to map full grain-size distributions, but the transition between radar-smooth sand surfaces and radar-rough gravels can be assessed, and trends in these bedload arrangements are visible. Longer wavelength SAR (e.g., L-band) shows a larger range of measurement, and higher spatial resolution SAR (e.g., TerraSAR-X/TanDEM-X) can be used for detailed geomorphic characterization. Mapping the sand-gravel transitions in alluvial rivers can be done using even shorter wavelength and coarse spatial-resolution SAR sensors (such as from freely available Sentinel-1 C-band imagery). The methods presented here increase the breadth of environmental measurements possible from spaceborne radar. The spatial scales of these observations can be greatly increased to entire orogenic belts, and time series, such as those regularly generated from Sentinel-1, can potentially be used to look at temporal dynamics of sand and gravel bedload.

CRediT authorship contribution statement

Benjamin Purinton: Project administration, Investigation, Methodology, Writing - original draft.**Bodo Bookhagen:** Project administration, Funding acquisition, Formal analysis, Writing - review & editing.

Declaration of competing interest

The authors declare that they have no known competing financial interests or personal relationships that could have appeared to influence the work reported in this paper.

Acknowledgments

The authors thank the DLR for TerraSAR-X/TanDEM-X scenes received through proposal XTI_GEO16727 to B. Bookhagen. Project funding was sourced from DFG funded IRTG-StRATEGy (IGK2018) and NEXUS funded through the MWFK Brandenburg, Germany, both for B. Bookhagen. Detailed reviews from Tom Farr and one anonymous reviewer greatly improved the manuscript's structure and the clarity of our analyses.

Appendix A. Supplementary data

Supplementary data to this article can be found online at <https://doi.org/10.1016/j.rse.2020.111799>.

References

- Allmendinger, R.W., Jordan, T.E., Kay, S.M., Isacks, B.L., 1997. The evolution of the Altiplano-Puna Plateau of the Central Andes. *Annu. Rev. Earth Planet. Sci.* 25, 139–174. <https://doi.org/10.1146/annurev.earth.25.1.139>.
- Arrell, K., Wise, S., Wood, J., Donoghue, D., 2008. Spectral filtering as a method of visualising and removing striped artefacts in digital elevation data. *Earth Surf. Process. Landf.* 33, 943–961. <https://doi.org/10.1002/esp.1597>.
- Attal, M., Lavé, J., 2006. Changes of bedload characteristics along the Marsyandi River (Central Nepal): implications for understanding hillslope sediment supply, sediment load evolution along fluvial networks, and denudation in active orogenic belts. *Geol. Soc. Am. Spec. Pap.* 398, 143–171. [https://doi.org/10.1130/2006.2398\(09\)](https://doi.org/10.1130/2006.2398(09)).
- Attal, M., Mudd, S., Hurst, M., Weinman, B., Yoo, K., Naylor, M., 2015. Impact of change in erosion rate and landscape steepness on hillslope and fluvial sediments grain size in the Feather River basin (Sierra Nevada, California). *Earth Surf. Dyn.* 3, 201–222. <https://doi.org/10.5194/esurf-3-201-2015>.
- Aubert, M., Baghdadi, N., Zribi, M., Douaoui, A., Loumagne, C., Baup, F., Hajj, M.E., Garrigues, S., 2011. Analysis of TerraSAR-X data sensitivity to bare soil moisture, roughness, composition and soil crust. *Remote Sensing of Environment* 115, 1801–1810. URL: <http://www.sciencedirect.com/science/article/pii/S003442571100071X>. 1016/j.rse.2011.02.021.
- Baade, J., Schmullius, C.C., 2010. Interferometric microrelief sensing with TerraSAR-X first results. *IEEE Trans. Geosci. Remote Sens.* 48, 965–970. <https://doi.org/10.1109/TGRS.2009.2036720>.
- Baghdadi, N., Zribi, M., 2006. Evaluation of radar backscatter models IEM, Oh and Dubois using experimental observations. *Int. J. Remote Sens.* 27, 3831–3852. URL: [doi:10.1080/01431160600658123](https://doi.org/10.1080/01431160600658123). <https://doi.org/10.1080/01431160600658123>.
- Baghdadi, N., Zribi, M., Loumagne, C., Ansart, P., Anguela, T.P., 2008. Analysis of TerraSAR-X data and their sensitivity to soil surface parameters over bare agricultural fields. *Remote Sensing of Environment* 112, 4370–4379. URL: <http://www.sciencedirect.com/science/article/pii/S0034425708002496>. 1016/j.rse.2008.08.004.
- Baghdadi, N., El Hajj, M., Choker, M., Zribi, M., Bazzi, H., Vaudour, E., Gilliot, J.-M., Ebengo, D.M., 2018. Potential of sentinel-1 images for estimating the soil roughness over bare agricultural soils. *Water* 10. <https://doi.org/10.3390/w10020131>. URL: <https://www.mdpi.com/2073-4441/10/2/131>.
- Bookhagen, B., Strecker, M.R., 2008. Orographic barriers, high-resolution TRMM rainfall, and relief variations along the Eastern Andes. *Geophys. Res. Lett.* 35. <https://doi.org/10.1029/2007gl032011>.
- Bookhagen, B., Strecker, M.R., 2012. Spatiotemporal trends in erosion rates across a pronounced rainfall gradient: examples from the southern Central Andes. *Earth Planet. Sci. Lett.* 327–328, 97–110. <https://doi.org/10.1016/j.epsl.2012.02.005>.
- Booth, A.M., Roering, J.J., Perron, J.T., 2009. Automated landslide mapping using spectral analysis and high-resolution topographic data: Puget Sound lowlands, Washington, and Portland Hills, Oregon. *Geomorphology* 109, 132–147. <https://doi.org/10.1016/j.geomorph.2009.02.027>.
- Bousbih, S., Zribi, M., Lili-Chabaane, Z., Baghdadi, N., El Hajj, M., Gao, Q., Mougenot, B., 2017. Potential of sentinel-1 radar data for the assessment of soil and cereal cover parameters. *Sensors* 17. <https://doi.org/10.3390/s17112617>. URL: <https://www.mdpi.com/1424-8220/17/11/2617>.
- Bryant, R., Moran, M.S., Thoma, D.P., Holifield Collins, C.D., Skirvin, S., Rahman, M., Slocum, K., Starks, P., Bosch, D., Gonzalez Dugo, M.P., 2007. Measuring surface roughness height to parameterize radar backscatter models for retrieval of surface soil moisture. *IEEE Geosci. Remote Sens. Lett.* 4, 137–141. <https://doi.org/10.1109/LGRS.2006.887146>.
- Campbell, B.A., 2001. Radar backscatter from mars: Properties of rock-strewn surfaces. *Icarus* 150, 38–47. URL: <http://www.sciencedirect.com/science/article/pii/S0019103500965667>. <https://doi.org/10.1006/icar.2000.6566>.
- Campbell, B.A., Shepard, M.K., 1996. Lava flow surface roughness and depolarized radar scattering. *Journal of Geophysical Research: Planets* 101, 18941–18951. URL: <https://agupubs.onlinelibrary.wiley.com/doi/abs/10.1029/95JE01804>. <https://doi.org/10.1029/95JE01804>.
- Castino, F., Bookhagen, B., Strecker, M., 2016a. Rainfall variability and trends of the past six decades (1950–2014) in the subtropical NW Argentine Andes. *Clim. Dyn.* 3, 1049–1067. <https://doi.org/10.1007/s00382-016-3127-2>.
- Castino, F., Bookhagen, B., Strecker, M., 2016b. River-discharge dynamics in the southern Central Andes and the 1976–77 global climate shift. *Geophys. Res. Lett.* 43. <https://doi.org/10.1002/2016GL070868>.
- Castino, F., Bookhagen, B., Strecker, M.R., 2017. Oscillations and trends of river discharge in the southern Central Andes and linkages with climate variability. *J. Hydrol.* 555, 108–124. <https://doi.org/10.1016/j.jhydrol.2017.10.001>.
- Church, M., 2002. Geomorphic thresholds in riverine landscapes. *Freshw. Biol.* 47, 541–557.
- Deroïn, J., Company, A., Simonin, A., 1997. An empirical model for interpreting the relationship between backscattering and arid land surface roughness as seen with the SAR. *IEEE Trans. Geosci. Remote Sens.* 35, 86–92. <https://doi.org/10.1109/36.551937>.
- Dierking, W., 1999. Quantitative roughness characterization of geological surfaces and implications for radar signature analysis. *IEEE Trans. Geosci. Remote Sens.* 37, 2397–2412. <https://doi.org/10.1109/36.789638>.
- Dingle, E.H., Attal, M., Sinclair, H.D., 2017. Abrasion-set limits on Himalayan gravel flux. *Nature* 544, 471–474. <https://doi.org/10.1038/nature22039>.
- Evans, D.L., Farr, T.G., Ford, J.P., Thompson, T.W., Werner, C.L., 1986. Multipolarization radar images for geologic mapping and vegetation discrimination. *IEEE Trans. Geosci. Remote Sens.* GE-24, 246–257. <https://doi.org/10.1109/TGRS.1986.289644>.
- Evans, D.L., Farr, T.G., van Zyl, J.J., 1992. Estimates of surface roughness derived from synthetic aperture radar (SAR) data. *IEEE Trans. Geosci. Remote Sens.* 30, 382–389. <https://doi.org/10.1109/36.134087>.
- Farr, T., 1993. Guide to Magellan Image Interpretation. Chapter Chapter 5: Radar Interactions With Geologic Surfaces. Jet Propulsion Laboratory, California Institute of Technology, La Caada Flintridge, CA, USA. URL: <https://history.nasa.gov/JPL-93-24/ch5.htm>.
- Farr, T.G., Chadwick, O.A., 1996. Geomorphic processes and remote sensing signatures of alluvial fans in the Kun Lun Mountains, China. *Journal of Geophysical Research: Planets* 101, 23091–23100. URL: <https://agupubs.onlinelibrary.wiley.com/doi/abs/10.1029/96JE01603>. <https://doi.org/10.1029/96JE01603> arXiv: <https://agupubs.onlinelibrary.wiley.com/doi/pdf/10.1029/96JE01603>.
- Fisher, G.B., Bookhagen, B., Amos, C.B., 2013. Channel planform geometry and slopes from freely available high-spatial resolution imagery and DEM fusion: implications

- for channel width scalings, erosion proxies, and fluvial signatures in tectonically active landscapes. *Geomorphology* 194, 46–56. <https://doi.org/10.1016/j.geomorph.2013.04.011>.
- GDAL/OGR contributors, 2019. GDAL/OGR Geospatial Data Abstraction Software Library. Open Source Geospatial Foundation URL: <https://gdal.org>.
- Gorrab, A., Zribi, M., Baghdadi, N., Mougenot, B., Chabaane, Z.L., 2015. Potential of X-band TerraSAR-X and COSMO-SkyMed sAR data for the assessment of physical soil parameters. *Remote Sensing* 7, 747–766. URL: <https://www.mdpi.com/2072-4292/7/1/747>. <https://doi.org/10.3390/rs70100747>.
- Grant, G.E., 2012. The geomorphic response of gravel-bed rivers to dams: perspectives and prospects. In: Gravel-Bed Rivers. Wiley-Blackwell, pp. 165–181. <https://doi.org/10.1002/9781119952497.ch15>, chapter 15.
- Hetz, G., Mushkin, A., Blumberg, D.G., Baer, G., Ginat, H., 2016. Estimating the age of desert alluvial surfaces with spaceborne radar data. *Remote Sensing of Environment* 184, 288–301. URL: <http://www.sciencedirect.com/science/article/pii/S0034425716302632>. [10.1016/j.rse.2016.07.006](https://doi.org/10.1016/j.rse.2016.07.006).
- Hilley, G.E., Strecker, M.R., 2005. Processes of oscillatory basin filling and excavation in a tectonically active Orogen: Quebrada del Toro basin, NW Argentina. *Geol. Soc. Am. Bull.* 117, 887–901. <https://doi.org/10.1130/B25602.1>.
- Hwang, P.A., Fois, F., 2015. Surface roughness and breaking wave properties retrieved from polarimetric microwave radar backscattering. *Journal of Geophysical Research: Oceans* 120, 3640–3657. URL: <https://agupubs.onlinelibrary.wiley.com/doi/abs/10.1002/2015JC010782> arXiv: <https://agupubs.onlinelibrary.wiley.com/doi/pdf/10.1002/2015JC010782>.
- Jarvis, A., Reuter, H.I., Nelson, A., Guevara, E., et al., 2008. Hole-filled SRTM for the globe version 4. available from the CGIAR-CSI SRTM 90m Database. <http://srtm.cgiar.org>.
- Kankaku, Y., Suzuki, S., Osawa, Y., 2013. Alos-2 mission and development status. In: 2013 IEEE International Geoscience and Remote Sensing Symposium-IGARSS. IEEE, pp. 2396–2399. <https://doi.org/10.1109/IGARSS.2013.6723302>.
- Kierein-Young, K., 1997. The integration of optical and radar data to characterize mineralogy and morphology of surfaces in Death Valley, California, U.S.A. *Int. J. Remote Sens.* 18, 1517–1541. <https://doi.org/10.1080/014311697218250>.
- Kondolf, G.M., Wolman, M.G., 1993. The sizes of salmonid spawning gravels. *Water Resour. Res.* 29, 2275–2285. <https://doi.org/10.1029/93WR00402>.
- Krieger, G., Moreira, A., Fiedler, H., Hajnsek, I., Werner, M., Younis, M., Zink, M., 2007. TanDEM-X: a satellite formation for high-resolution SAR interferometry. *IEEE Trans. Geosci. Remote Sens.* 45, 3317–3341. <https://doi.org/10.1109/TGRS.2007.900693>.
- Lamb, M.P., Venditti, J.G., 2016. The grain size gap and abrupt gravel-sand transitions in rivers due to suspension fallout. *Geophys. Res. Lett.* 43, 3777–3785. <https://doi.org/10.1002/2016GL068713>.
- Marrett, R., Allmendinger, R., Alonso, R., Drake, R., 1994. Late Cenozoic tectonic evolution of the Puna Plateau and adjacent foreland, Northwestern Argentine Andes. *J. S. Am. Earth Sci.* 7, 179–207.
- McCauley, J.F., Schaber, G.G., Breed, C.S., Grolier, M.J., Haynes, C.V., Issawi, B., Elachi, C., Blom, R., 1982. Subsurface valleys and geoarcheology of the Eastern Sahara revealed by shuttle radar. *Science* 218, 1004–1020. URL: <https://science.sciencemag.org/content/218/4576/1004>. <https://doi.org/10.1126/science.218.4576.1004> full.pdf. arXiv: <https://science.sciencemag.org/content/218/4576/1004.full.pdf>.
- Mushkin, A., Gillespie, A., 2005. Estimating sub-pixel surface roughness using remotely sensed stereoscopic data. *Remote Sensing of Environment* 99, 75–83. URL: <http://www.sciencedirect.com/science/article/pii/S003442570500177X>. [10.1016/j.rse.2005.02.018](https://doi.org/10.1016/j.rse.2005.02.018) (Scientific Results from ASTER).
- Mushkin, A., Gillespie, A.R., 2006. Mapping sub-pixel surface roughness on mars using high-resolution satellite image data. *Geophysical Research Letters* 33. URL: <https://agupubs.onlinelibrary.wiley.com/doi/abs/10.1029/2006GL027095>. <https://doi.org/10.1029/2006GL027095> arXiv: <https://agupubs.onlinelibrary.wiley.com/doi/pdf/10.1029/2006GL027095>.
- Nelson, P.A., Venditti, J.G., Dietrich, W.E., Kirchner, J.W., Ikeda, H., Iseyama, F., Sklar, L.S., 2009. Response of bed surface patchiness to reductions in sediment supply. *J. Geophys. Res. Earth Surf.* 114. <https://doi.org/10.1029/2008JF001144>.
- Peake, W., Oliver, T., 1971. The response of terrestrial surfaces at microwave frequencies. In: Technical Report AFAL-TR-70-301 U.S. Air Force Avionics Lab.
- Perron, J.T., Kirchner, J.W., Dietrich, W.E., 2008. Spectral signatures of characteristic spatial scales and nonfractal structure in landscapes. *J. Geophys. Res. Earth Surf.* 113. <https://doi.org/10.1029/2007JF000866>.
- Pfeiffer, A.M., Finnegan, N.J., Willenbring, J.K., 2017. Sediment supply controls equilibrium channel geometry in gravel rivers. *Proc. Natl. Acad. Sci.* 114, 3346–3351.
- Purinton, B., Bookhagen, B., 2017. Validation of digital elevation models (DEMs) and comparison of geomorphic metrics on the Southern Central Andean Plateau. *Earth Surface Dynamics* 5, 211–237. URL: <https://www.earth-surf-dynam.net/5/211/2017>. <https://doi.org/10.5194/esurf-5-211-2017>.
- Purinton, B., Bookhagen, B., 2018. Measuring decadal vertical land-level changes from SRTM-C (2000) and TanDEM-X (~2015) in the South-Central Andes. *Earth Surf. Dyn.* 6, 971–987. <https://doi.org/10.5194/esurf-6-971-2018>.
- Purinton, B., Bookhagen, B., 2019a. Introducing PebbleCounts: a grain-sizing tool for photo surveys of dynamic gravel-bed rivers. *Earth Surface Dynamics* 7, 859–877. URL: <https://www.earth-surf-dynam.net/7/859/2019/>. <https://doi.org/10.5194/esurf-7-859-2019>.
- Purinton, B., Bookhagen, B., 2019b. PebbleCounts: A Python Grain-Sizing Algorithm for Gravel-Bed River Imagery. <https://doi.org/10.5880/fidgeo.2019.007>. URL: <https://github.com/UP-RS-ESP/PebbleCounts>.
- Rahman, M., Moran, M., Thoma, D., Bryant, R., Collins, C.H., Jackson, T., Orr, B., Tischler, M., 2008. Mapping surface roughness and soil moisture using multi-angle radar imagery without ancillary data. *Remote Sensing of Environment* 112, 391–402. URL: <http://www.sciencedirect.com/science/article/pii/S0034425707003008>. [10.1016/j.rse.2006.10.026](https://doi.org/10.1016/j.rse.2006.10.026) (Soil Moisture Experiments 2004 (SMEX04) Special Issue).
- Rice, S., Church, M., 1998. Grain size along two gravel-bed rivers: statistical variation, spatial pattern and sedimentary links. *Earth Surf. Process. Landf.* 23, 345–363. [https://doi.org/10.1002/\(SICI\)1096-9837\(199804\)23:4<345::AID-ESP850>3.0.CO;2-B](https://doi.org/10.1002/(SICI)1096-9837(199804)23:4<345::AID-ESP850>3.0.CO;2-B).
- Ridley, J., Strawbridge, F., Card, R., Phillips, H., 1996. Radar backscatter characteristics of a desert surface. *Remote Sensing of Environment* 57, 63–78. URL: <http://www.sciencedirect.com/science/article/pii/0034425796000181>. [10.1016/0034-4257\(96\)00018-1](https://doi.org/10.1016/0034-4257(96)00018-1).
- Sadeh, Y., Cohen, H., Maman, S., Blumberg, D.G., 2018. Evaluation of manning α TM's n roughness coefficient in arid environments by using SAR backscatter. *Remote Sens.* 10<https://doi.org/10.3390/rs10101505>. URL: <https://www.mdpi.com/2072-4292/10/10/1505>.
- Shepard, M.K., Campbell, B.A., Bulmer, M.H., Farr, T.G., Gaddis, L.R., Plaut, J.J., 2001. The roughness of natural terrain: A planetary and remote sensing perspective. *Journal of Geophysical Research: Planets* 106, 32777–32795. URL: <https://agupubs.onlinelibrary.wiley.com/doi/abs/10.1029/2000JE001429>. <https://doi.org/10.1029/2000JE001429>.
- Sklar, L.S., Dietrich, W.E., Foufoula-Georgiou, E., Lashermes, B., Bellugi, D., 2006. Do gravel bed river size distributions record channel network structure? *Water Resour. Res.* 42, W06D18. <https://doi.org/10.1029/2006WR005035>.
- Small, D., 2011. Flattening gamma: radiometric terrain correction for SAR imagery. *IEEE Trans. Geosci. Remote Sens.* 49, 3081–3093. <https://doi.org/10.1109/TGRS.2011.2120616>.
- SNAP, E., 2019. Snap software. URL: <https://step.esa.int/main/toolboxes/snap/>.
- Srivastava, H.S., Patel, P., Sharma, Y., Navalagund, R.R., 2009. Large-area soil moisture estimation using multi-incidence-angle radarsat-1 SAR data. *IEEE Trans. Geosci. Remote Sens.* 47, 2528–2535. <https://doi.org/10.1109/TGRS.2009.2018448>.
- Strecker, M., Alonso, R., Bookhagen, B., Carrapa, B., Hilley, G., Sobel, E., Trauth, M., 2007. Tectonics and climate of the Southern Central Andes. *Annu. Rev. Earth Planet. Sci.* 35, 747–787. <https://doi.org/10.1146/annurev.earth.35.031306.140158>.
- Svitik, J.P., Vörösmarty, C.J., Kettner, A.J., Green, P., 2005. Impact of humans on the flux of terrestrial sediment to the global coastal ocean. *Science* 308, 376–380.
- Tofelde, S., Schildgen, T.F., Savi, S., Pingel, H., Wickert, A.D., Bookhagen, B., Wittmann, H., Alonso, R.N., Cottle, J., Strecker, M.R., 2017. 100 kyr fluvial cut-and-fill terrace cycles since the Middle Pleistocene in the Southern Central Andes, NW Argentina. *Earth Planet. Sci. Lett.* 473, 141–153. <https://doi.org/10.1016/j.epsl.2017.06.001>.
- Torres, R., Snoeij, P., Geudtner, D., Bibby, D., Davidson, M., Attema, E., Potin, P., Rommen, B., Flouri, N., Brown, M., Traver, I.N., Deghaye, P., Duesmann, B., Rosich, B., Miranda, N., Bruno, C., L'Abbate, M., Croci, R., Pietropaolo, A., Huchler, M., Rostan, F., 2012. GMES sentinel-1 mission. *Remote Sensing of Environment* 120, 9–24. URL: <http://www.sciencedirect.com/science/article/pii/S0034425712000600>. [10.1016/j.rse.2011.05.028](https://doi.org/10.1016/j.rse.2011.05.028) (The Sentinel Missions - New Opportunities for Science).
- Uddin, K., Matin, M.A., Meyer, F.J., 2019. Operational flood mapping using multi-temporal sentinel-1 SAR images: a case study from Bangladesh. *Remote Sens.* 11<https://doi.org/10.3390/rs11131581>. URL: <https://www.mdpi.com/2072-4292/11/13/1581>.
- Ulaby, F.T., Moore, R.K., Fung, A.K., 1982. *Microwave Remote Sensing, Volumes 1, 2, and 3*. Addison-Wesley, pp. 2162.
- Verhoest, N.E., Lievens, H., Wagner, W., lvarez Mozos, J., Moran, M.S., Mattia, F., 2008. On the soil roughness parameterization problem in soil moisture retrieval of bare surfaces from synthetic aperture radar. *Sensors* 8, 4213–4248. URL: <https://www.mdpi.com/1424-8220/8/7/4213>. <https://doi.org/10.3390/s8074213>.
- Vreugdenhil, M., Wagner, W., Bauer-Marschallinger, B., Pfeil, I., Teubner, I., Rdiger, C., Strauss, P., 2018. Sensitivity of sentinel-1 backscatter to vegetation dynamics: an Austrian case study. *Remote Sens.* 10<https://doi.org/10.3390/rs10091396>. URL: <https://www.mdpi.com/2072-4292/10/9/1396>.
- Walter, R.C., Merritts, D.J., 2008. Natural streams and the legacy of water-powered mills. *Science* 319, 299–304.
- Weeks, R.J., Smith, M., Pak, K., Li, W.-H., Gillespie, A., Gustafson, B., 1996. Surface roughness, radar backscatter, and visible and near-infrared reflectance in Death Valley, California. *Journal of Geophysical Research: Planets* 101, 23077–23090. URL: <https://agupubs.onlinelibrary.wiley.com/doi/abs/10.1029/96JE01247>. <https://doi.org/10.1029/96JE01247> arXiv: <https://agupubs.onlinelibrary.wiley.com/doi/pdf/10.1029/96JE01247>.
- Weeks, R., Smith, M., Pak, K., Gillespie, A., 1997. Inversions of SIR-C and AIRSAR data for the roughness of geological surfaces. *Remote Sensing of Environment* 59, 383–396. URL: <http://www.sciencedirect.com/science/article/pii/S0034425796001617>. [10.1016/S0034-4257\(96\)00161-7](https://doi.org/10.1016/S0034-4257(96)00161-7) (Spaceborne Imaging Radar Mission).
- Williams, K.K., Greeley, R., 2004. Laboratory and field measurements of the modification of radar backscatter by sand. *Remote Sensing of Environment* 89, 29–40. URL: <http://www.sciencedirect.com/science/article/pii/S003442570300258X>. [10.1016/j.rse.2003.09.006](https://doi.org/10.1016/j.rse.2003.09.006).
- Wolcott, J., Church, M., 1991. Strategies for sampling spatially heterogeneous phenomena; the example of river gravels. *J. Sediment. Res.* 61, 534–543. <https://doi.org/10.1029/D426753-2B26-11D7-8648000102C1865D>.